2 Interferometric Synthetic Aperture Radar (InSAR) Study of Coastal Wetlands Over Southeastern Louisiana

Zhong Lu and Oh-Ig Kwoun

CONTENTS

2.1 INTRODUCTION

Coastal wetlands constitute important ecosystems in terms of flood control, water and nutrient storage, habitat for fish and wildlife reproduction and nursery activities, and overall support of the food chain [1]. Louisiana has one of the largest expanses of coastal wetlands in the conterminous United States, and these wetlands contain an extraordinary diversity of habitats. The unique habitats along the Gulf of Mexico, complex hydrological connections, and migratory routes of birds, fish, and other species place Louisiana's coastal wetlands among the nation's most productive and important natural assets [2].

The balance of Louisiana's coastal systems has been upset by a combination of natural processes and human activities. Massive coastal erosion probably started around 1890, and about 20% of the coastal lowlands (mostly wetlands) have eroded in the past 100 years [3]. For example, the loss rate due to erosion for Louisiana's coastal wetlands was as high as 12,202 and 6194 ha/year in the 1970s and 1990s, respectively [4]. Marked environmental changes have had significant impacts on Louisiana's coastal ecosystems, including effects from frequent natural disasters such as the hurricanes Katrina and Rita in 2005 and Ike in 2008. Therefore, an effective method of mapping and monitoring coastal wetlands is essential to understand the current status of these ecosystems and the influence of environmental changes and human activities on them. In addition, it has been demonstrated that measurement of changes in water level in wetlands and, consequently, of changes in water storage capacity provides a governing parameter in hydrologic models and is required for comprehensive assessment of flood hazards (e.g., [5]). Inaccurate knowledge of floodplain storage capacity in wetlands can lead to significant errors in hydrologic simulation and modeling [5]. *In situ* measurement of water levels over wetlands is cost-prohibitive, and insufficient coverage of stage recording instruments results in poorly constrained estimates of the water storage capacity of wetlands [6]. With frequent coverage over wide areas, satellite sensors may provide a cost-effective tool to accurately measure water storage.

A unique characteristic of synthetic aperture radar (SAR) in monitoring wetlands over cloud-prone subtropical regions is the all-weather and day-and-night imaging capability. The SAR backscattering signal is composed of intensity and phase components. The intensity component of the signal is sensitive to terrain slope, surface roughness, and the dielectric constant of the target being imaged. Many studies have demonstrated that SAR intensity images can be used to map and monitor forested and nonforested wetlands occupying a range of coastal and inland settings (e.g., [7–9]). Most of those studies relied on the fact that, when standing water is present beneath the vegetation canopies, the radar backscattering signal intensity changes with water-level changes, depending on vegetation type and structure. As such, SAR intensity data have been used to monitor flooded and dry conditions, temporal variations in the hydrological conditions of wetlands, and classification of wetland vegetation at various geographic settings [7,10–23].

The phase component of the signal is related to the apparent distance from the satellite to ground resolution elements as well as the interaction between radar waves and scatterers within a resolution element of the imaged area. Interferometric SAR (InSAR) processing can then produce an interferogram using the phase components of

two SAR images of the same area acquired from similar vantage points at different times. An interferogram depicts range changes between the radar and the ground and can be further processed with a digital elevation model (DEM) to produce an image of ground deformation at a horizontal resolution of tens of meters over large areas and centimeter to subcentimeter vertical precision under favorable conditions (e.g., [24,25]). InSAR has been extensively utilized to study ground surface deformation associated with volcanic, earthquake, landslide, and land subsidence processes [24,26].

Alsdorf et al. [27,28] found that interferometric analysis of L-band (wavelength = 24 cm) Shuttle Imaging Radar-C (SIR-C) and Japanese Earth Resources Satellite (JERS-1) SAR imagery can yield centimeter-scale measurements of water-level changes throughout inundated floodplain vegetation. Their work confirmed that scattering elements for L-band radar consist primarily of the water surface and vegetation trunks, which allows double-bounce backscattering returns as illustrated in Section 2.3.2 of this chapter. Later, Wdowinski et al. [29] applied L-band JERS-1 images to map water-level changes over the Everglades in Florida. All these studies rely on this common understanding: flooded forests permit double-bounce returns of L-band radar pulses, which allow maintaining InSAR coherence—a parameter quantifying the degree of changes in backscattering characteristics (see Sections 2.3.2 and 2.6 for details). Loss of coherence renders an InSAR image useless to retrieve meaningful information about surface movement. However, it is commonly recognized that the shorter wavelength radar, such as C-band (wavelength = 5.7 cm), backscatters from the upper canopy of swamp forests rather than the underlying water surface, and that a double-bounce backscattering can only occur over inundated macrophytes and small shrubs [14,30–32]. As a consequence, C-band radar images were not exploited to study water-level changes beneath swamp forests until 2005, when Lu et al. [33] found that C-band InSAR images could maintain coherence over wetlands to allow estimates of water-level change.

The primary objectives of this study are to utilize multitemporal C-band SAR images from different sensors to differentiate vegetation types over coastal wetlands and explore the potential utility of C-band InSAR imagery for mapping water-level changes. SAR data acquired from two sensors during several consecutive years are used to address these objectives.

The rest of the chapter is composed of seven sections. The study site is introduced in Section 2.2. Section 2.3 describes the fundamental background of the SAR backscattering mechanism and the relationship between InSAR phase measurements and water-level changes. Section 2.4 describes SAR data, calibration, processing, and InSAR processing. Section 2.5 describes temporal variations of radar backscattering signal over different vegetation classes and their usefulness to infer vegetation structures. Section 2.5 also evaluates the relationship between radar backscattering coefficients and normalized difference vegetation index values derived from optical images to provide additional information to differentiate wetland classes. In Section 2.6, interferometric coherence measurements are systematically analyzed for different vegetation types, seasonality, and time separation. In Section 2.7, we present the InSAR-derived water-level changes over swamp forests and discuss the associated potentials and challenges of our approach. Section 2.8 provides discussions and conclusion. Although this chapter largely explores C-band radar images for wetland

mapping and water dynamics, a few L-band images are introduced in Section 2.8 to highlight the potential of integrating C-band and L-band images for improved vegetation and water mapping.

2.2 STUDY SITE

The study area is over southeastern Louisiana (Figure 2.1) and includes the western part of New Orleans and the area between Baton Rouge and Lafayette. The area primarily consists of eight land-cover types: urban, agriculture, bottomland forest, swamp forest, freshwater marsh, intermediate marsh, brackish marsh, and saline marsh. Agriculture and urban land cover are found in higher elevation areas and along the levees. Bottomland forests exist in less frequently flooded, lower elevation areas and along the lower perimeter of the levee system, while swamp forests are in the lowest elevation areas. Bottomland forests are dry during most of the year, while swamp forests are inundated. Both types of forests are composed largely of American elm, sweetgum, sugarberry, swamp red maple, and bald cypress [23,34].

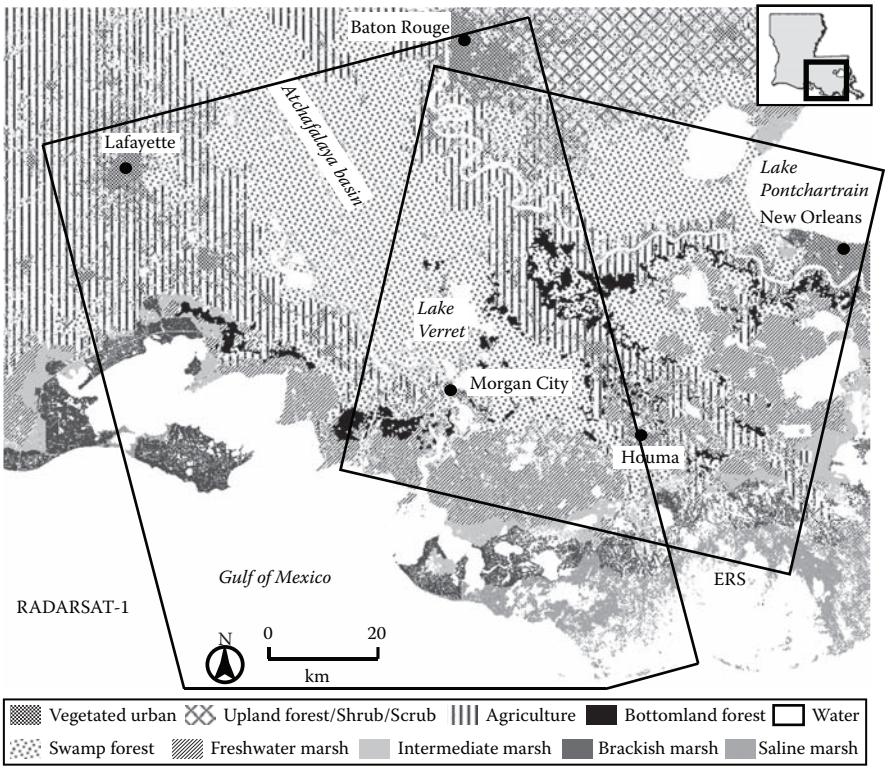

FIGURE 2.1 **(See color insert following page xxx.)** Thematic map. Modified from GAP and 1990 USGS National Wetland Research Center classification results, showing major land-cover classes of the study area. Polygons represent extents of SAR images shown in Figure 2.3 for the ERS-1/ERS-2 and RADARSAT-1 tracks.

The freshwater marshes (Figure 2.1) are composed largely of floating vegetation. Maidencane, spikerush, and bulltongue are the dominant species. Freshwater marshes have the greatest plant diversity and the highest soil organic matter content of any marsh type throughout the study area [35]. However, plant diversity varies with location, and many areas of monotypic marshes are found in the Louisiana coastal zone. The salinity of freshwater marshes ranges from 0 to 3 ppt [3,34].

With a salinity level of 2–5 ppt, intermediate marshes (Figure 2.1) represent a zone of mild salt content that results in fewer plant species than freshwater marshes have [35]. The intermediate marsh is characterized by plant species common to freshwater marshes but with higher salt-tolerant versions of them toward the sea. Intermediate marshes are largely composed of bulltongue and saltmeadow cordgrass [3]. The latter, also called wire grass, is not found in freshwater marshes [36].

Brackish marshes (Figure 2.1) are characterized by a salinity range of 4–15 ppt and are irregularly flooded by tides; they are largely composed of wire grass and three-square bullrush. This marsh community virtually contains all wire grass—clusters of three-foot-long grass-like leaves with little variation in plant species [36].

Saline marshes (Figure 2.1) have the highest salinity concentrations (12 ppt and higher) [3]. With the least diversity of vegetation species, saline marshes are largely composed of smooth cordgrass, oyster grass, and saltgrass.

The hydrology of marsh areas produces freshwater marshes in relatively low-energy environments, which are potentially subject to tidal changes but not ebb and flow. They change slowly and have thick sequences of organic soils or floating grass root mats. Saline and brackish marshes are found in high-energy areas and are subject to the ebb and flow of the tides [3].

2.3 RADAR MAPPING OF WETLANDS

2.3.1 Possible Radar Backscattering Mechanisms Over Wetlands

Over vegetated terrain, the incoming radar wave interacts with various elements of the vegetation as well as the ground surface. Part of the energy is attenuated, and the rest is scattered back to the antenna. The amount of radar energy returned to the antenna (backscattering signal) depends on the size, density, shape, and dielectric constant of the target, as well as SAR system characteristics, such as incidence angle, polarization, and wavelength. The dielectric constant, or permittivity, describes how a surface attenuates or transmits the incoming radar wave. Live vegetation with high water content has a higher dielectric constant than drier vegetation, implying that a stronger backscattering signal is expected from wet vegetation than drier vegetation. The transmission of the radar signal through the canopy is also directly related to the characteristics of the radar as well as the canopy structure. Therefore, comparing the backscattering values (σ°) from various vegetation canopies in diverse environments can provide insight into the dominant canopy structure.

Radar signal backscattering mechanisms over wetlands are simplified into four major categories: *surface backscattering*, *volume backscattering*, *double-bounced backscattering*, and *specular scattering*. Figure 2.2 illustrates how different structural layers of vegetation affect the way a radar signal returns. Forested wetlands

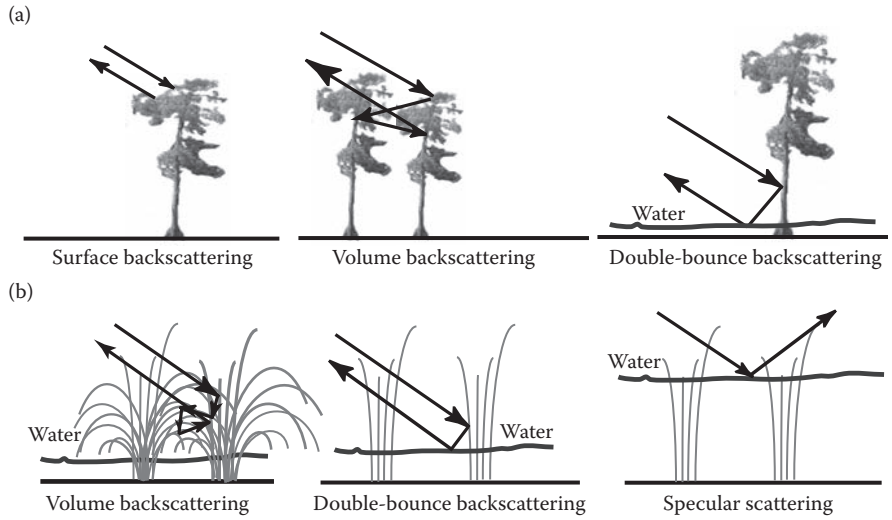

FIGURE 2.2 Schematic figures showing the contributions of radar backscattering over (a) forests and (b) marshes due to canopy surface backscattering, canopy volume backscattering, specular scattering, and double-bounce backscattering.

often develop into distinct layers, such as an overstory of dominant tree species, an understory of companion trees and shrubs, and a ground layer of herbaceous plants [37]. Therefore, over a dense forest, the illuminating radar signal scatters from the canopy surface, and a fraction of the energy is returned to the antenna. This phenomenon is called *surface backscattering*. The remaining radar wave penetrates into and interacts with the vegetation volume, and a portion of the energy is returned to the antenna. This results in *volume backscattering*. Volume backscattering can also dominate moderately dense forests with dense understory (Figure 2.2a). In a moderately dense forested canopy, some microwave energy penetrates through the overstory and interacts with tree trunks and the ground layer. If the ground is flooded, a large portion of the microwave energy is forward-scattered off the tree trunks, bounced off the smooth water surface, and then back to the radar antenna. This phenomenon is called *double-bounced backscattering* (Figure 2.2a). Because double-bounced backscattering returns more microwave energy back to the antenna than other types of backscattering, the SAR image should have an enhanced intensity compared to other types of vegetation canopy where volumetric backscattering dominates.

Over herbaceous canopies, SAR can often penetrate through the vegetation to reach the ground surface depending on the vegetation density. If the soil is dry, multiple backscatterings between vegetation and the ground surface can attenuate the incoming radar signal, reducing the energy returned to the radar. If the soil is wet, the higher dielectric constant of the soil reduces the transmission of the radar wave and enhances the backscattering return. If the ground is flooded, and the above-water stems are large enough and properly oriented to allow double bounce between the water surface and stems, the backscattering signal is significantly enhanced (i.e., double-bounced backscattering) (Figure 2.2b). If the ground is completely flooded,

and the vegetation canopy is almost submerged, there is little chance for the radar signal to interact with the canopy stems and the water surface. Instead, most of the radar energy is scattered away from the antenna (i.e., *specular scattering*) (Figure 2.2b) and little energy is bounced back to the radar. Floating aquatic vegetation and short vegetation in flooded areas may exhibit similar backscattering returns and are therefore indistinguishable from SAR backscattering values. In general, the overall bulk density of these vegetation classes may determine the total amount of SAR signal potentially backscattered to the sensor.

2.3.2 Mapping Water-Level Changes Using InSAR

Interactions of C-band radar waves with water surface are relatively simple [38]. As SAR transmits radar pulses at an off-nadir look-angle, if the weather is calm, a smooth open-water surface causes most of the radar energy to reflect away from the radar sensor, resulting in little energy being returned to the SAR receiver. When the open-water surface is rough and turbulent, part of the radar energy can be scattered back to the sensor. However, SAR signals over open water are not coherent if two radar images are acquired at different times. Thus, it has been generally accepted that InSAR is an inappropriate tool to use in studying changes in the water level of open water. As described in the previous section, the radar backscattering over flooded wetlands consists of contributions from the interactions of radar waves with the canopy surface, canopy volume, and water surface. Neglecting specular scattering, the total radar backscattering over wetlands can be approximated as the incoherent summation of contributions from (a) canopy surface backscattering, (b) canopy volume backscattering that includes backscattering from multiple path interactions of canopy water, and (c) double-bounce trunk-water backscattering (Figure 2.2a). The relative contributions from those three backscattering components are controlled primarily by vegetation type, vegetation structure (and canopy closure), seasonal conditions, and other environmental factors. Over marsh wetlands, the primary backscattering mechanism is volume backscattering with possible contributions from stalk-water double-bounce backscattering, or specular scattering if the aboveground vegetation is short and the majority of the imaged surface is water (Figure 2.2b).

Ignoring the atmospheric delay in SAR data acquired at two different times, and assuming that topographic effect is removed, the repeat-pass interferometric phase (ϕ) is approximately the incoherent summation of differences in surface backscattering phase (ϕ_s), volume backscattering phase (ϕ_v), and double-bounce backscattering phase (ϕ_d):

$$\phi = (\phi_{s2} - \phi_{s1}) + (\phi_{v2} - \phi_{v1}) + (\phi_{d2} - \phi_{d1}), \tag{2.1}$$

where ϕ_{s1}, ϕ_{v1}, and ϕ_{d1} are the surface, volume, and double-bounce backscattering phase values from the SAR image acquired at an early date, and ϕ_{s2}, ϕ_{v2}, and ϕ_{d2} are the corresponding phase values from the SAR image acquired at a later date. **Q1**

As the two SAR images are acquired at different times, the loss of interferometric coherence requires evaluation. Only when coherence is maintained are

interferometric phase values useful to map water-level changes. Loss of InSAR coherence is often referred to as decorrelation. Besides the thermal decorrelation caused by the presence of uncorrelated noise sources in radar instruments, there are three primary sources of decorrelation over wetlands (e.g., [9,39,40]): (a) geometric decorrelation resulting from imaging a target from different look angles, (b) volume decorrelation caused by volume backscattering effects, and (c) temporal decorrelation due to environmental changes over time.

Geometric decorrelation increases as the baseline—the distance between satellites—increases, until a critical length is reached when coherence is lost (e.g., [41,42]). For surface backscattering, most of the effect of baseline geometry on the measurement of interferometric coherence can be removed by common spectral band filtering [43]. Volume backscattering describes multiple scattering of the radar pulse occurring within a distributed volume of vegetation; therefore, InSAR baseline geometry configuration can significantly affect volume decorrelation. Volume decorrelation is most often coupled with geometric decorrelation and is a complex function of vegetation canopy structure that is difficult to simulate. As a result, volume decorrelation cannot be removed. Generally, the contribution of volume backscattering is controlled by the proportion of transmitted signal that penetrates the surface and the relative two-way attenuation from the surface to the volume element and back to the sensor [9]. Canopy closure may significantly impact volume backscattering; the volume decorrelation should generally be disproportional to canopy closure. Both surface backscattering and volume backscattering consume and attenuate the transmitted radar signal; hence, they reduce the proportion of radar signal available to produce double-bounce backscattering that is utilized to measure water-level changes [44].

Temporal decorrelation describes any event that changes the physical orientation, composition, or scattering characteristics and spatial distribution of scatterers within an imaged volume. Temporal decorrelation is the net effect of changes in radar backscattering and therefore depends on the stability of the scatterers, the canopy penetration depth of the transmitted pulse, and the response to changing conditions with respect to the wavelength. Over wetlands, these decorrelations are primarily caused by wind changing leaf orientation, moisture condensation, rain, and seasonal phenology changing the dielectric constant of the vegetation, flooding changing the dielectric constant and roughness of the canopy background, as well as anthropogenic activities such as cultivation and timber harvesting [9,44].

The above discussion has clarified how the geometric, volume, and temporal decorrelation are interleaved with each other and collectively affect InSAR coherence over wetlands. The combined decorrelation estimated using InSAR images (quantitatively assessed in Section 6.2) determines the ability to detect water-level changes through radar double-bounce backscattering. When double-bounce backscattering dominates the returning radar signal, a repeat-pass InSAR image is potentially coherent enough to allow the measurement of water-level changes from the interferometric phase values. The interferometric phase (ϕ) is related to the water-level change (Δh) by the following relationship [44]: **Q2**

$$\Delta h = -\frac{\lambda\phi}{4\pi \cos\theta} + n, \tag{2.2}$$

where ϕ is the interferogram phase value, λ is the SAR wavelength (5.66 cm for C-band ERS-1, ERS-2, and RADARSAT-1), θ is the SAR local incidence angle, and n is the noise caused primarily by the aforementioned decorrelation effects.

2.4 DATA AND PROCESSING

2.4.1 SAR Data

SAR data used in the study consist of 33 scenes of European Remote Sensing (ERS)-1 and ERS-2 images and 19 scenes of RADARSAT-1 images (Table 2.1). The ERS-1/ERS-2 scenes, spanning 1992–1998, are from the descending track 083 with a radar incidence angle of about 20°–26°. The ERS-1/ERS-2 data are vertical-transmit and vertical-receive (VV) polarized. The RADARSAT-1 scenes, spanning 2002–2004, are from an ascending track with a radar incidence angle of about 25°–31°. Unlike ERS-1/ERS-2, RADARSAT-1 images are horizontal-transmit and horizontal-receive (HH) polarized. SAR raw data are processed into single-look complex (SLC) images with antenna pattern compensation. The intensity of the SLC image was converted into the backscattering coefficient, σ°, according to Wegmüller and Werner [45]. Southern Louisiana's topography is almost flat; therefore, additional adjustment of σ° for local terrain slope effect is not necessary.

ERS-1 and ERS-2 SLC images are coregistered to a common reference image using a two-dimensional *sinc* function [45]. The coregistered ERS SLC images are multilooked using a 2×10 window to represent a ground-projected pixel size of about 40×40 m^2. The same procedure is used to process RADARSAT-1 data

TABLE 2.1
SAR Sensor Characteristics: Sensor, Band, Orbit Direction, and Incidence Angle

Satellite	Image Acquisition Dates (year: mm/dd)
ERS-1 (C-band, VV)	1992: 06/11, 07/16, 08/20, 09/24, 10/29
Orbit pass: Descending	1993: 01/07, 04/22, 09/09
Incidence angle: 23.3°	1995: 11/11
	1996: 01/20, 05/04 (11 scenes)
ERS-2 (C-VV)	1995: 11/12, 12/17
Orbit pass: Descending	1996: 01/21, 05/05, 06/09, 07/14, 08/18, 09/22, 10/27, 12/01
Incidence angle: 23.3°	1997: 01/05, 03/16, 05/25, 09/07, 10/12, 11/16
	1998: 01/25, 03/01, 04/05, 07/19, 08/23, 09/27 (22 scenes)
RADARSAT-1 (C-HH)	2002: 05/03, 05/27, 06/20, 07/14, 08/07, 08/31, 11/11
Orbit pass: Ascending	2003: 02/15, 05/22, 06/15, 07/09, 08/02, 10/12, 12/23
Incidence angle: 27.7°	2004: 02/09, 03/28, 04/21, 07/02, 09/12 (19 scenes)
PALSAR (L-HH)	2007: 02/27, 04/14 (2 scenes)
Orbitpa ss: Ascending	
Incidencea ngle:38.7°	

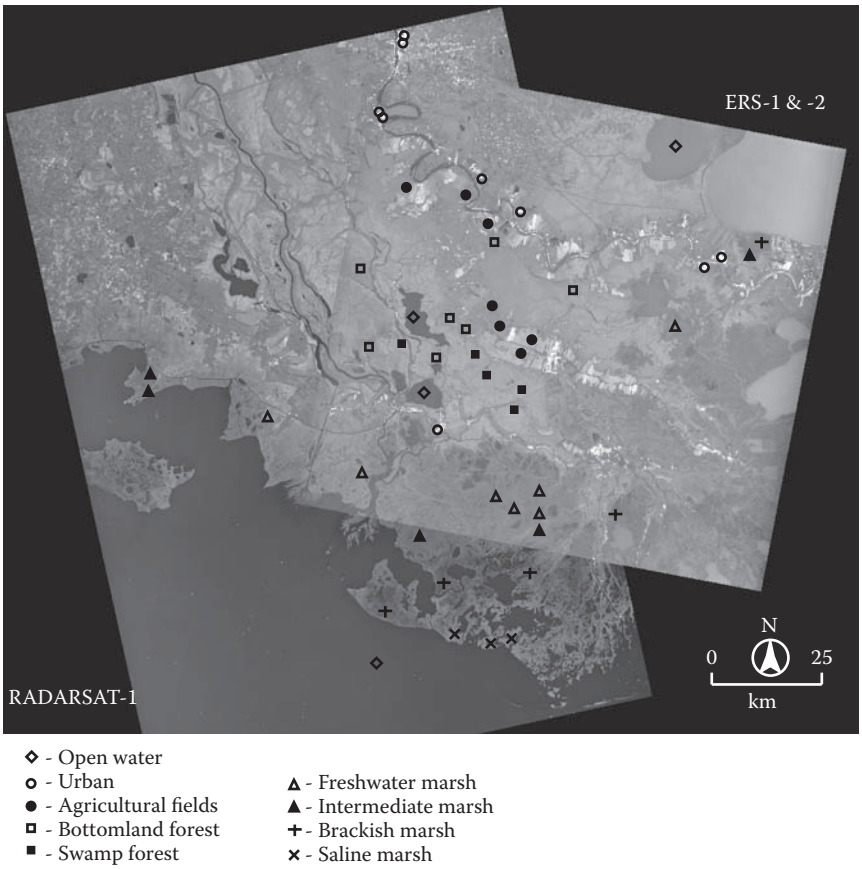

FIGURE 2.3 Averaged ERS-1/ERS-2 and RADARSAT-1 intensity images showing locations where quantitative coherence analyses are conducted.

(Table 2.1). All coregistered RADARSAT-1 images are multilooked with a 3×10 window to represent a ground-projected pixel size of about 50×50 m^2. Speckle noise in the images is suppressed using the Frost adaptive despeckle filter [46] with a 3×3 window size on the coregistered and multilooked images. Finally, SAR images are georeferenced and coregistered with the modified GAP land-cover map (Figure 2.1) [23]. A SAR image mosaic composed of both the ERS-1/ERS-2 and RADARSAT-1 images is shown in Figure 2.3.

2.4.2 SAR Data Calibration

Many data samples across the study area were selected to examine seasonal variations of σ° for different vegetation types. Locations of data samples are shown in Figure 2.3. For each of the nine land-cover classes, between three and nine locations distributed across the study area were chosen for backscattering analysis. The 2004

Digital Orthophoto Quarter Quadrangle (DOQQ) imagery for Louisiana [47] is used to verify the land-cover type over the sampling sites. The size of the sampling boxes varies between 3×3 and 41×41 pixels so that each box covers only a single land-cover type. The DOQQ imagery is also used to ensure the homogeneity of land cover at each site.

The results of average σ° for each class are shown in Figure 2.4. The overall difference in the average σ° between Figure 2.4a and b is due to differences in sensors and environmental change. The σ°_{ERS} shows a generally downward trend (Figure 2.4a). This long-term declination is present for all land-cover classes, suggesting that ERS-2 has a temporal decrease of antenna power at a rate of about 0.5 dB per year, similar to the report by Meadows et al. [48]. Therefore, this long-term declination of σ° has been compensated before further analysis.

Unlike ERS, $\sigma^\circ_{RADARSAT}$ exhibits strong temporal variation for all land-cover types (Figure 2.4b), which is particularly evidenced by the observation that $\sigma^\circ_{RADARSAT}$ over water mimics the variation of σ° over other land classes. This strongly suggests that the temporal variation in RADARSAT-1 is caused not only by changes in environmental conditions but also by some systematic changes that are not well understood. Such variations warrant removal prior to any further analysis of σ°.

Extensive homogeneous surfaces with known backscattering characteristics, such as the Amazon forests, or carefully designed corner reflectors, are ideal for radiometric calibration, but no such locations exist in our study site. However, many artificial structures and objects in cities, such as buildings, roads, and industrial facilities, may be considered corner-reflector units and behave like permanent scatterers whose backscattering characteristics do not change with time despite environmental variation [49]. Under ideal conditions, backscattering coefficients from urban areas should remain almost constant over time and therefore usable as an alternative to calibrate time-varying radar backscattering characteristics. This led Kwoun and Lu [23] to propose a relative calibration of radar backscattering coefficients for vegetation classes using σ° over urban areas: for each SAR scene, the averaged σ° value of urban areas from the corresponding image is used as the reference and subtracted from σ° values of other land-cover classes in that individual image. The "calibrated" σ°s are then used to study backscattering characteristics of different land-cover types and their seasonal changes (Figure 2.5). Figure 2.6 shows seasonally averaged σ° of each land-cover type for leaf-on and leaf-off seasons after relative calibration.

2.4.3 InSAR Processing

A total of 47 ERS-1/ERS-2 interferograms with perpendicular baselines less than 300 m (Figure 2.7a) and 31 RADARSAT-1 interferograms with perpendicular baselines less than 400 m (Figure 2.7b) were produced. The common spectral band filtering is applied to maximize interferometric coherence [43]. Interferometric coherence was calculated using 15×15 pixels on ERS-1/ERS-2 interferograms that were generated with a multilook factor of 2×10 from the SLC images, and 11×11 pixels for RADARSAT-1 interferograms with a multilook factor of 3×11. Therefore, the coherence measurements were made over a spatial scale of about 600×600 m^2. As significant fringes were observed over swamp forest areas, we "detrended" the

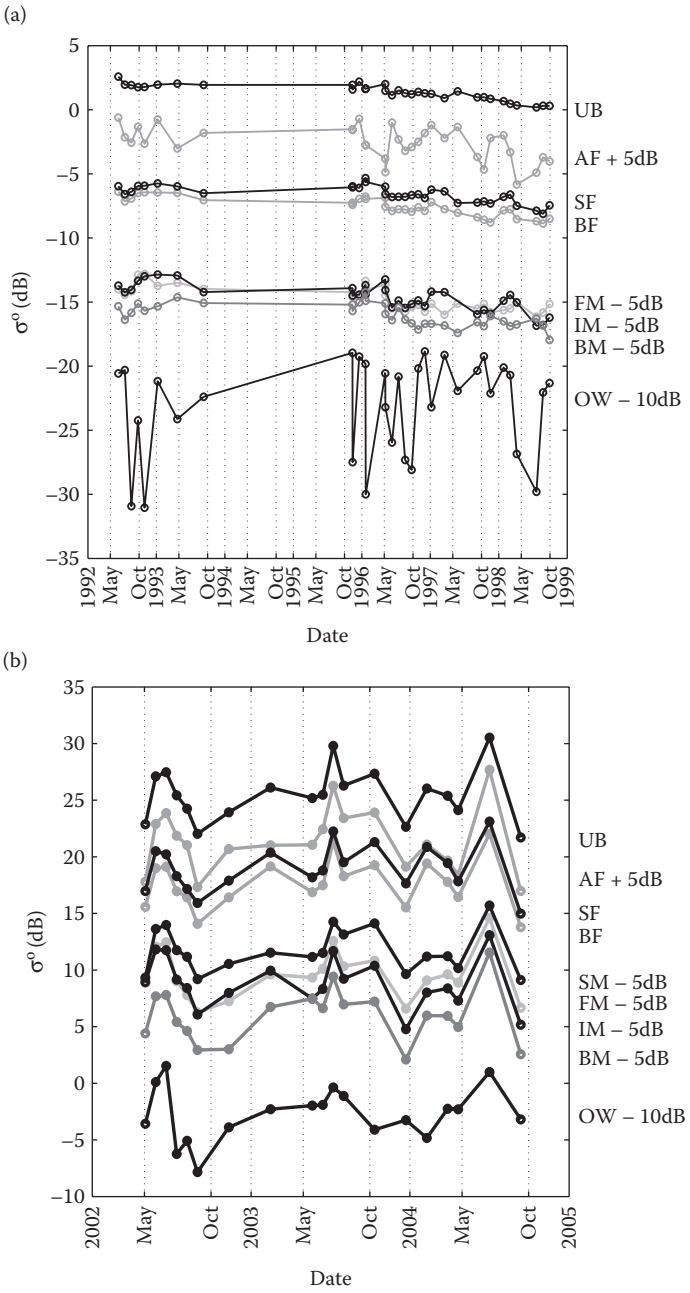

FIGURE 2.4 Temporal variations of radar backscattering coefficient from (a) ERS-1 and ERS-2 and (b) RADARSAT-1. UB: urban, AF: agricultural fields, SF: swamp forests, BF: bottomland forests, FM: freshwater marshes, IM: intermediate marshes, BM: brackish marshes, SM: saline marshes, OW: open water.

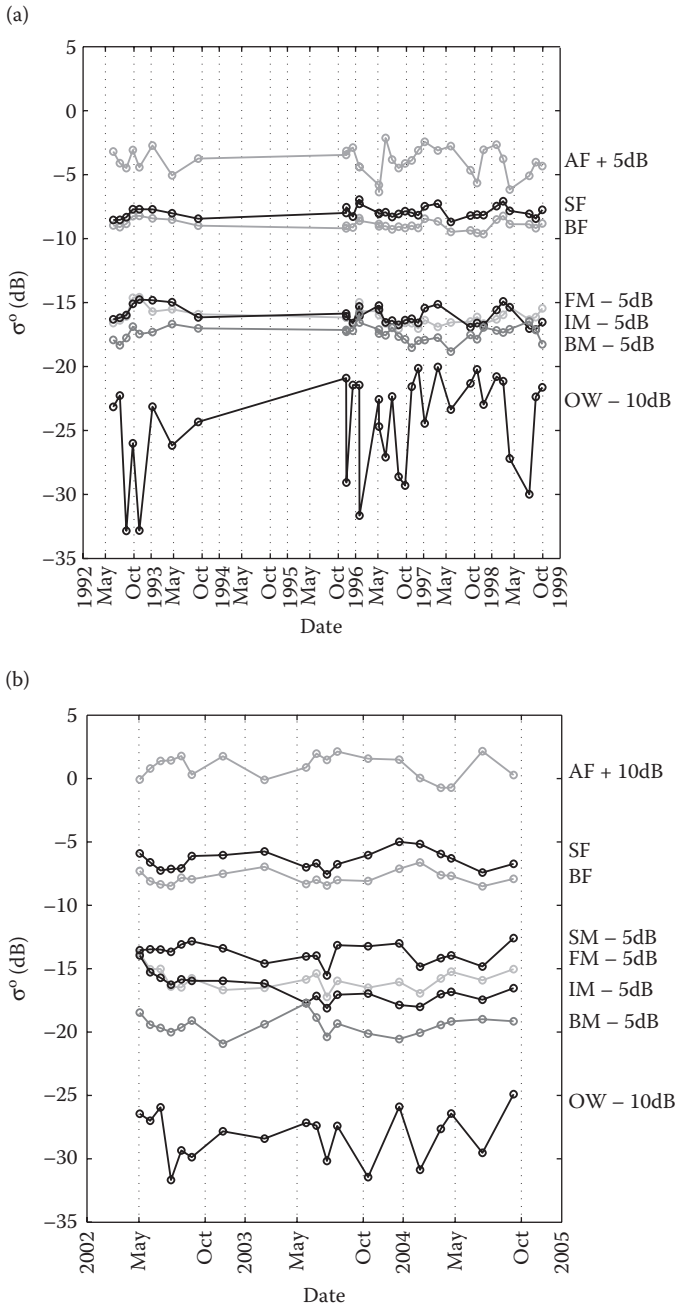

FIGURE 2.5 Calibrated radar backscattering coefficient (σ°) of each land-cover type from (a) ERS-1 and ERS-2 and (b) RADARSAT-1 images. The relative calibration is achieved with the averaged σ° of urban areas. AF: agricultural fields, SF: swamp forests, BF: bottomland forests, FM: freshwater marshes, IM: intermediate marshes, BM: brackish marshes, SM: saline marshes, OW: open water.

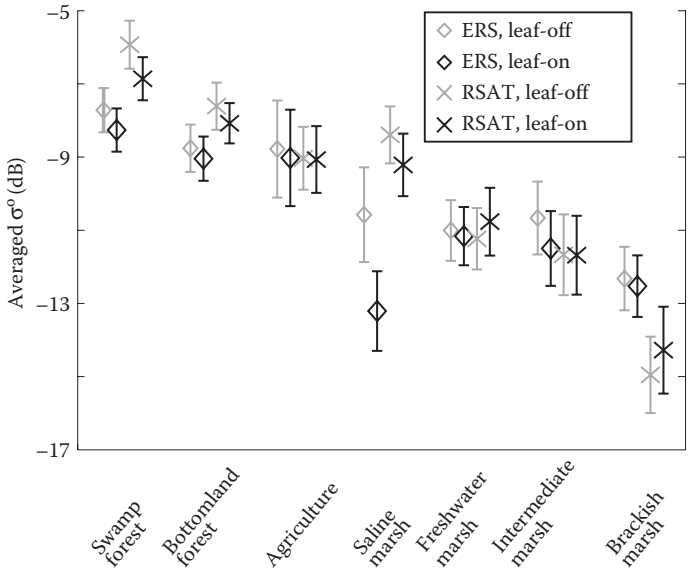

FIGURE 2.6 Multiyear seasonally averaged σ° of each land-cover type. The error bars represent 1 standard deviation.

fringes to calculate the coherence based on Lu and Kwoun's [44] procedure to reduce artifacts caused by dense fringes on the coherence estimation.

2.5 SAR BACKSCATTERING ANALYSIS

2.5.1 Radar Backscattering Over Different Land-Cover Classes

For the purpose of analyzing seasonal backscattering changes, a typical year is split into two seasons. As summarized in Section 2.5.2, the Normalized Difference Vegetation Index (NDVI) is used to identify the peaks of "green-up," which occur around early May and early October. For convenience, the period between May and October is referred to as the "leaf-on" season, and the rest of the year as the "leaf-off" season. However, our definition of "leaf-off" does not necessarily mean that the vegetation has no leaves, as one would expect of deciduous trees in high latitude regions. Over our study area, some marsh types exhibit little, if any, seasonal variation (e.g., black needlerush); others change in their green biomass percentage; and others completely overturn. The "calibrated" σ°s within a season are averaged to study backscattering characteristics of different land covers and their seasonal changes (Figure 2.6).

The agricultural fields in the study area do not follow the natural cycle of vegetation. Multiple harvests and plowing drastically change surface roughness and moisture conditions, which significantly alter radar backscattering values. Therefore, agricultural fields are excluded from further analysis.

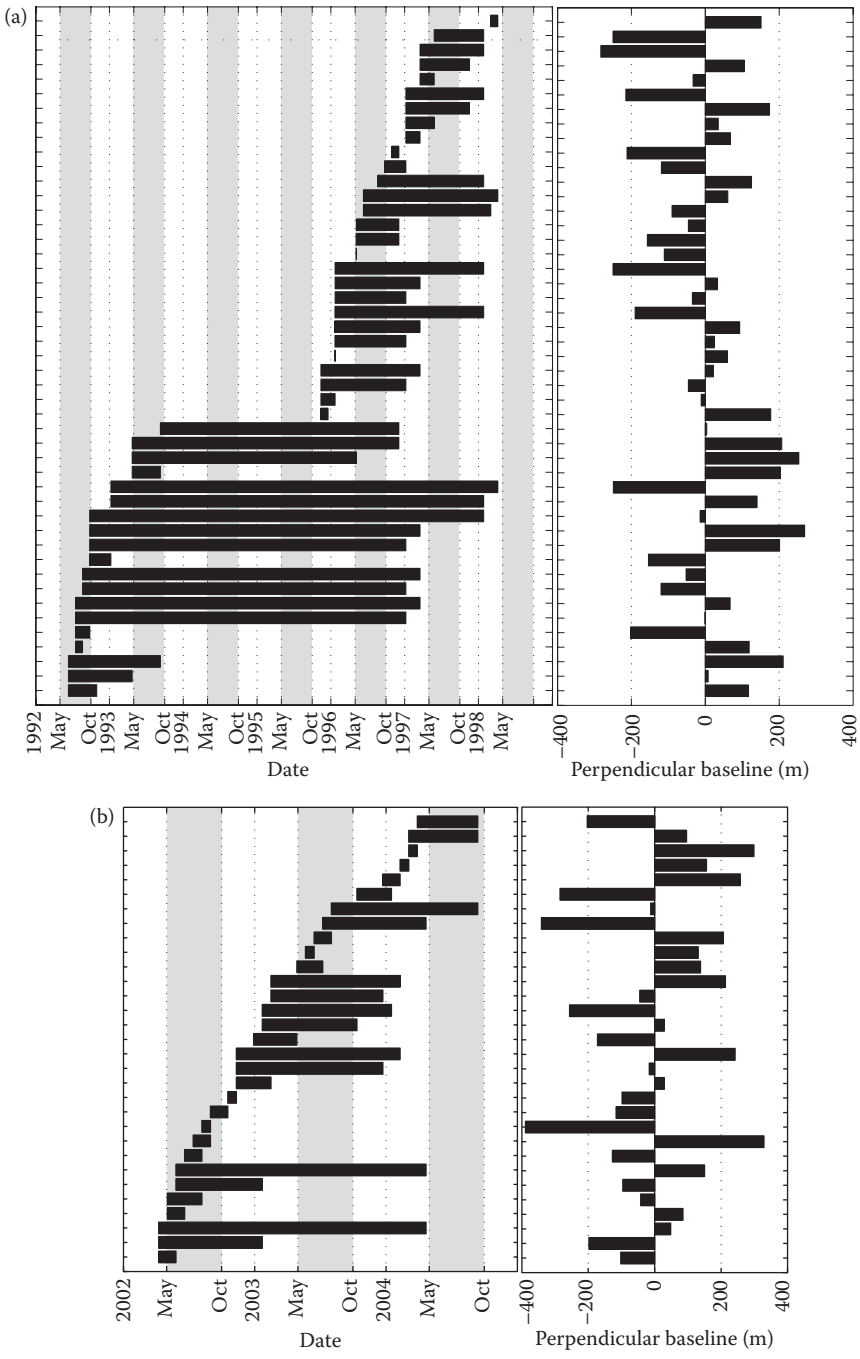

FIGURE 2.7 InSAR image pair characteristics, including image acquisition times and their corresponding baselines for both ERS-1/ERS-2 and RADARSAT-1 data used in this study.

The σ° values of swamp forests are the highest among all of the vegetation classes under investigation (Figure 2.6). This suggests that the density of trees is moderate or sparse enough, and the density of understory, if any, is low enough to allow penetration of the C-band SAR signal to interact with the water surface for double-bounce backscattering. The mean σ° values of swamp forests from ERS and RADARSAT-1 are about 0.5 and 0.9 dB higher during leaf-off seasons than during leaf-on seasons, respectively. Seasonal backscatter changes over swamp forests are consistently larger than those of bottomland forests. This is probably because during the leaf-on season, radar attenuation at the overstory is increased and double-bounced backscattering is reduced, which results in decreases in both σ° values and interferometric coherence. The $\sigma^\circ_{\text{RADARSAT}}$ during leaf-on season is around 0.9 dB higher than the $\sigma^\circ_{\text{ERS}}$ during leaf-off season.

The bottomland forest has the second highest mean σ° values (Figure 2.6). The averaged σ° of bottomland forests is consistently lower than that of swamp forests by 0.5–1.3 dB for ERS and 0.8–1.7 dB for RADARSAT-1, indicating weaker radar signal return from bottomland forest than swamp forest. This is attributed to the decreased double-bounced backscattering due to dense understory canopy, which is abundant in bottomland forests. Similar to the swamp forests, the averaged $\sigma^\circ_{\text{LEAF\_OFF}}$ is slightly higher than the averaged $\sigma^\circ_{\text{LEAF\_ON}}$; however, the difference is much smaller over bottomland forests than swamp forests. From a land-cover classification perspective, comparison of σ° between bottomland and swamp forests indicates that averaged intensity of RADARSAT-1 data during any single year contains sufficient information to differentiate the two classes (Figure 2.6).

Freshwater and intermediate marshes show relatively similar σ° for both ERS and RADARSAT-1. The seasonally averaged values of $\sigma^\circ_{\text{ERS}}$ and $\sigma^\circ_{\text{RADARSAT}}$ for freshwater marshes do not show any distinct trends (Figure 2.6). As for intermediate marshes, the mean values of $\sigma^\circ_{\text{ERS}}$ during leaf-off season are 0.9–1.5 dB higher than during leaf-on season, except for 1996; however, the averaged $\sigma^\circ_{\text{RADARSAT}}$ values do not show any consistent trends. From a land-cover classification perspective, Figure 2.6 indicates that freshwater marshes and intermediate marshes may not be easily distinguishable based on SAR backscattering signals. Also worth noting is that although fresh and intermediate marshes are outside the direct inundation of most tides, they could be flooded for extended time periods. In our analysis, those conditions are not included.

The seasonally averaged $\sigma^\circ_{\text{ERS}}$ of brackish marshes have the lowest mean σ° values (Figure 2.6). The drastic difference between ERS and RADARSAT is probably because sampling sites for the two sensors are not colocated due to a limitation in the image coverage (Figures 2.3 and 2.6). The averaged $\sigma^\circ_{\text{RADARSAT}}$ during leaf-on seasons is 0.8–0.9 dB higher than during leaf-off seasons, while $\sigma^\circ_{\text{ERS}}$ does not show any significant difference (Figure 2.6). From a land-cover classification perspective, Figure 2.6 indicates that single-year SAR data, particularly RADARSAT-1, are potentially sufficient to distinguish brackish marshes from other vegetation communities.

As in the case of brackish marshes, the sampling sites for RADARSAT and ERS data for saline marshes cannot be colocated (Figures 2.3 and 2.6). The mean $\sigma^\circ_{\text{ERS\_LEAF\_ON}}$ of saline marshes is comparable to that of brackish marshes, and the

mean $\sigma^{\circ}_{ERS\_LEAF\_OFF}$ shows considerably dynamic interseasonal change and is in the range of freshwater and intermediate marshes (Figure 2.6). The averaged $\sigma^{\circ}_{RADARSAT}$ is comparable to that of bottomland forests (Figure 2.6). Both ERS and RADARSAT data show that the averaged $\sigma^{\circ}_{LEAF\_OFF}$ is higher than the averaged $\sigma^{\circ}_{LEAF\_ON}$, as is the case with forests. The saline marsh community is inundated daily with salt water tides and is subjected to the ebb and flow of the tides [3]. Therefore, it provides a favorable condition for double-bounced scattering between stems and the water surface underneath. From the image classification perspective, RADARSAT data are probably sufficient to distinguish saline marshes from other marsh classes. The mean value of $\sigma^{\circ}_{ERS\_LEAF\_ON}$ of saline marshes is so distinct that some level of ambiguity in $\sigma^{\circ}_{RADARSAT}$ between bottomland forests and saline marshes can be resolved. In addition, the proximity to salt water is another potential indicator that separates these two communities.

In summary, to classify wetland classes over the study area, the seasonal σ° values averaged over multiple years are useful to distinguish among bottomland forests, swamp forests, saline marshes, brackish marshes, and freshwater and intermediate marshes. Forests versus marshes are identifiable because the $\sigma^{\circ}_{ERS\_LEAF\_ON}$ of marshes is significantly lower than that of forests. Swamp forests are marked with the highest σ° values from both ERS and RADARSAT-1.

Among the marshes, brackish marshes are characterized by the consistently lowest σ° of RADARSAT-1. A saline marsh may be identified by its highest averaged $\sigma^{\circ}_{RADARSAT}$ among marsh classes. Freshwater and intermediate marshes have very similar σ°. However, the averaged $\sigma^{\circ}_{ERS\_LEAF\_OFF}$ for intermediate marshes is marginally higher than $\sigma^{\circ}_{ERS\_LEAF\_ON}$. The seasonally averaged σ°s of both saline and brackish marshes behave quite distinctly compared to those of freshwater and intermediate marshes, which may help map changes in salinity in coastal wetlands.

2.5.2 SAR Backscattering versus Vegetation Index

The previous section has shown that seasonal variation of radar backscattering signals responds to changes in structural elements of vegetation classes. The seasonal changes of vegetation cover are also detectable by optical sensors. NDVI is a numerical indicator that utilizes the ratio between spectral reflectance measurements acquired in the red and near-infrared regions to assess whether the target being observed contains live green vegetation (e.g., [50]). We now show how the radar signal can be related to land-cover information derived from optical sensors by comparing σ° to NDVI derived from Advanced Very High Resolution Radiometer (AVHRR) imagery. The multiyear NDVI curves (Figure 2.8) are averaged into a single year to determine typical leaf-on and leaf-off seasons [23]. The peaks of averaged NDVI are found in the intervals of April 23–May 6 in the spring and September 24–October 7 in the fall; therefore, the time window from around May 1 until about the end of September is chosen as the "leaf-on" season. The leaf-on season is meant to represent the time when leaves maintain fully developed conditions and is characterized by peaks in the NDVI curves in the spring and fall (Figure 2.8). The rest of the year is defined as the "leaf-off" season.

Because the leaf-on season is the time period when leaves are fully developed, significant changes in radar backscattering are not expected. Regressions between

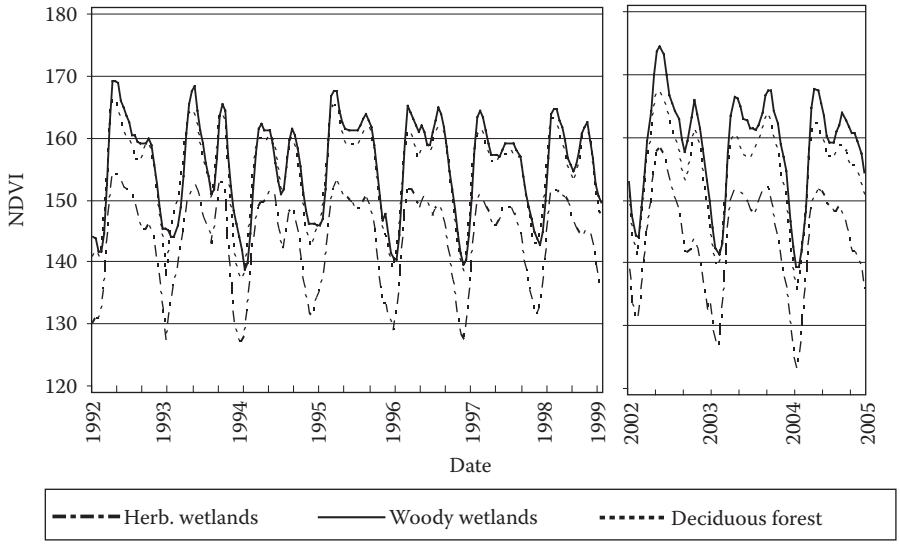

FIGURE 2.8 NDVI values adjusted for long-term trends during 1992–1998 and 2002–2004.

σ° and NDVI for all vegetation types do not show any significant correlation during leaf-on season because the dynamic range of the variation of NDVI is too narrow compared to radar backscatter changes. During the leaf-off season, both bottomland and swamp forests show moderate to strong negative correlations with NDVI (Figure 2.9a through d). The negative correlation during the leaf-off season is likely associated with the attenuation of radar backscatter due to the growth of leaves, which reduces the amount of radar signal available for double-bounce and volume scattering. As a result, radar backscatter decreases with the increase in NDVI for swamp and bottomland forests. Therefore, negative correlation between NDVI and σ° is anticipated.

For marshes, $\sigma^\circ_{\text{ERS\_LEAF\_OFF}}$ does not show any correlation with NDVI. However, $\sigma^\circ_{\text{RADARSAT\_LEAF\_OFF}}$ shows impressive positive correlation with NDVI (Figure 2.9e through h). This positive correlation implies that the radar backscattering is enhanced with an increase in NDVI, suggesting surface or volume scattering of the radar signal. For freshwater and intermediate marshes, positive correlation is consistent with our interpretation of σ° in Section 5.1. Brackish marshes show marginally positive correlation, which implies that brackish marshes are not as dense as the other marshes to enhance σ° sufficiently with the growth of vegetation. Saline marshes show moderate positive correlation. This may sound contradictory to our previous interpretation in Section 2.5.1. The increase in NDVI is probably associated with the thickening of saline marsh stems, which may be translated into an increase in the double-bounced radar backscattering signal. By combining NDVI and radar backscatter signal, forests versus wetland marshes are classifiable. NDVI maps derived from higher spatial resolution images and more detailed classes than those defined by NLCD may improve our current results.

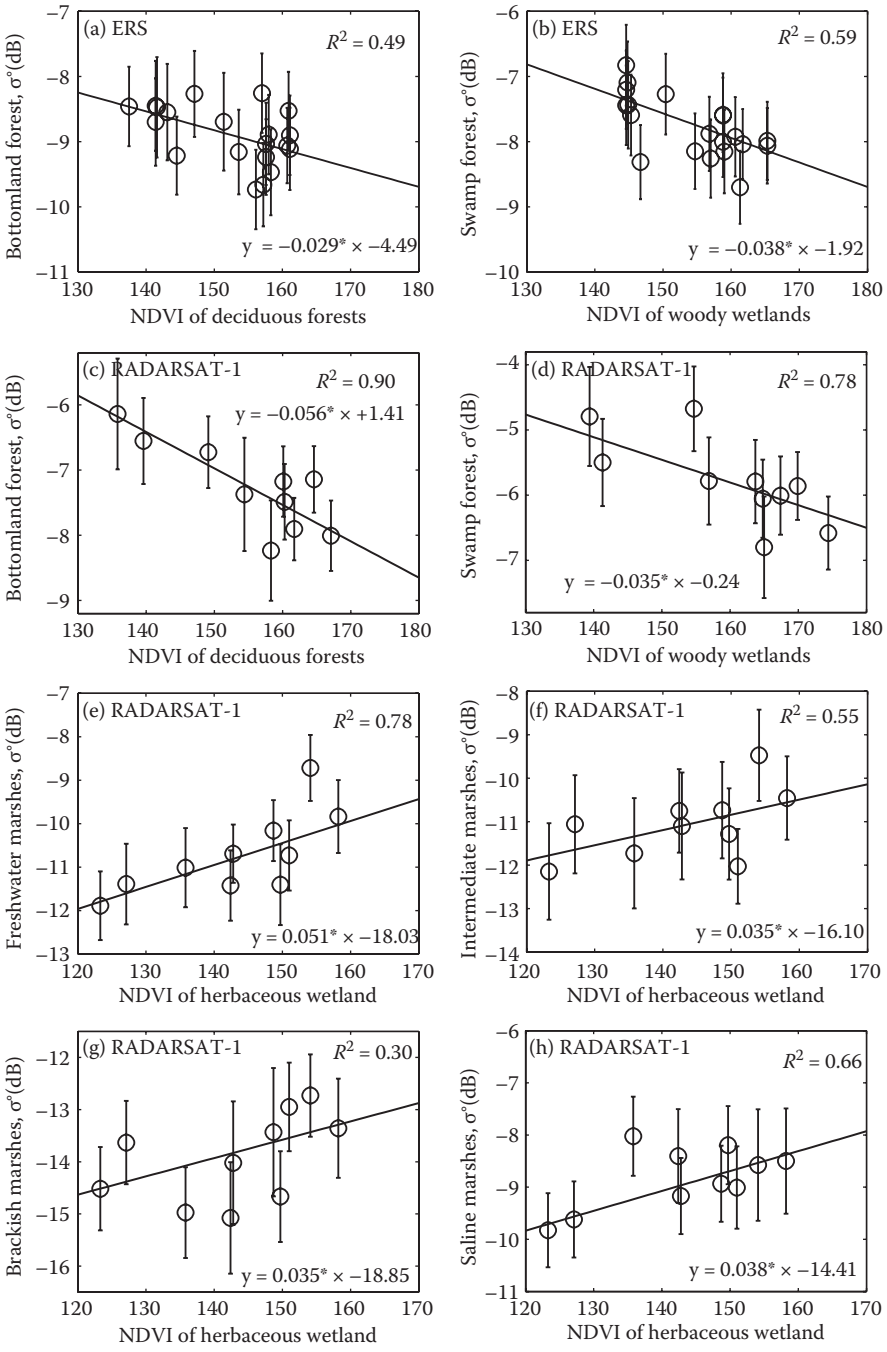

FIGURE 2.9 Regression modeling between calibrated ERS or RADARSAT-1 σ° and NDVI for the leaf-off season. ERS σ°s for marshes do not show any correlation with NDVIs and are therefore not presented in this figure.

2.6 InSAR COHERENCE ANALYSIS

2.6.1 Observed InSAR Images

A few examples of ERS-1/ERS-2 and RADARSAT-1 interferograms for portions of the study area are shown in Figure 2.10. Figure 2.10a through d shows ERS-1/ERS-2 interferograms acquired during leaf-off seasons, with a time separation of 1 day (Figure 2.10a), 35 days (Figure 2.10b), 70 days (Figure 2.10c), and 5 years (Figure 2.10d). The 1-day interferogram (Figure 2.10a) during the leaf-off season is coherent for almost every land-cover class except open water. In the 1-day interferogram, a few localized areas exhibit interferometric phase changes, which are most likely a result of water-level changes over the swamp forests. The large-scale phase changes over the southeastern part of the interferogram are likely caused by atmospheric delay anomalies. Most of the land-cover classes (Figure 2.1), except open water, bottomland forests, and some of the freshwater and intermediate marshes, are coherent in the 35-day interferogram (Figure 2.10b). The interferogram clearly shows the

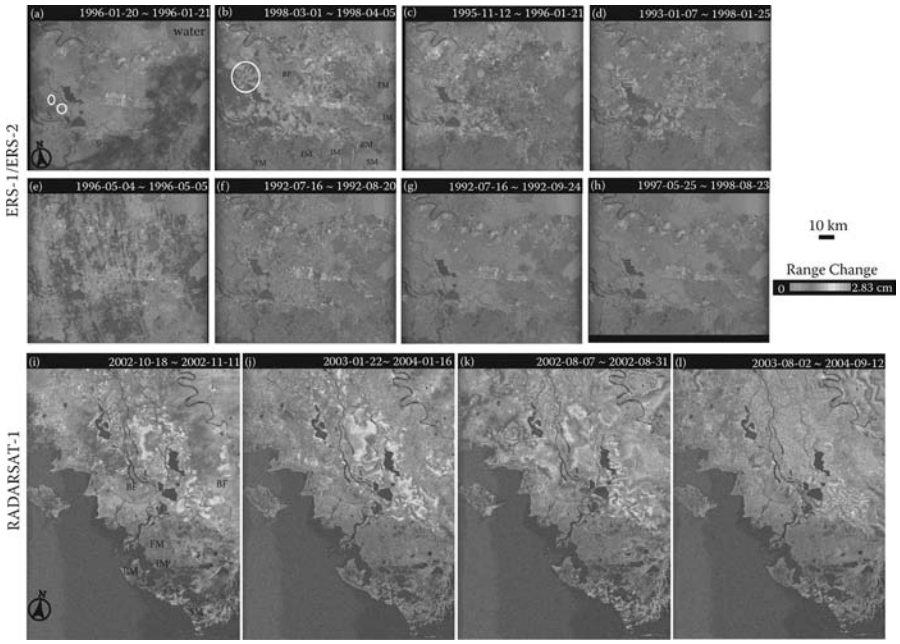

FIGURE 2.10 **(See color insert following page xxx.)** (a–d) ERS-1/ERS-2 InSAR images with different time separations during leaf-off seasons. (e–h) ERS-1/ERS-2 InSAR images with different time separations during leaf-on seasons. (i, j) RADARSAT-1 InSAR images during leaf-off seasons. (k, l) ERS-1/ERS-2 InSAR images during leaf-on seasons. Each fringe (full color cycle) represents 2.83 cm of range change between the ground and the satellite. The transition of colors from purple, red, yellow and green to blue indicates that the water level moved away from the satellite by an increasing amount in that direction. Random colors represent loss of InSAR coherence, where no meaningful range change information can be obtained from the InSAR phase values. AG: agricultural field, SF: swamp forest, BF: bottomland forest, FM: freshwater marsh, IM: intermediate marsh, BM: brackish marsh, SM: saline marsh, OW: open water.

water-level changes over both swamp forests and marshes (Figure 2.10b). The overall coherence for the 70-day interferogram (Figure 2.10c) is generally lower than the 35-day interferogram (Figure 2.10b). In 70 days (Figure 2.10c), bottomland forests, freshwater marshes, and intermediate marshes completely lose coherence, although some saline marshes and brackish marshes can maintain coherence. Over 5 years, some swamp forests and urban areas can maintain coherence (Figure 2.10d). Coherence can be maintained for swamp forests for over 5 years.

Figure 2.10e through h shows interferograms from ERS-1/ERS-2 SAR images acquired during leaf-on seasons, with a time separation of 1 day (Figure 2.10e), 35 days (Figure 2.10f), 70 days (Figure 2.10g), and 1 year (Figure 2.10h). Compared with the corresponding interferograms acquired during leaf-off seasons with similar time intervals (Figure 2.10a through d), the leaf-on interferograms generally exhibit much lower coherence. All the land-cover classes (Figure 2.1) maintain coherence in 1 day (Figure 2.10e). For most land-cover classes, except urban, agriculture, and portions of swamp forests, interferometric coherence cannot be maintained after 35 days (Figure 2.10f through h). With a time interval of 70 days, only urban and some agricultural fields have coherence (Figure 2.10g). Over 1 year, only urban areas maintain some degree of coherence (Figure 2.10h). The overall reduction in interferometric coherence for swamp forests during leaf-on seasons is because the dominant backscattering mechanism is not double-bounce backscattering but a combination of surface and volume backscattering.

Figure 2.10i and j shows two RADARSAT-1 interferograms acquired during leaf-off seasons. Interferometric coherence for the 24-day HH-polarization RADARSAT-1 interferogram (Figure 2.10i) is generally higher than the 35-day VV-polarization ERS-1/ERS-2 interferogram (Figure 2.10b). In 24 days, only water and some freshwater marshes do not have good coherence (Figure 2.10i). Bottomland forests (Figure 2.10i and j) can maintain good coherence for 24 days. From Figure 2.10j, it is obvious that some swamp forests and urban areas maintain coherence for more than 1 year.

Figure 2.10k and l shows RADARSAT-1 interferograms acquired during leaf-on seasons. Again, the 24-day HH-polarization RADARSAT-1 interferogram maintains higher coherence than the 35-day VV-polarization ERS-1/ERS-2 images (Figure 2.10f) for most land-cover types. The 1-year RADARSAT interferogram surprisingly is able to maintain relatively high coherence over parts of swamp forests and saline marshes in leaf-on seasons. In general, even though RADARSAT-1 coherence is reduced during leaf-on seasons, the reduction in coherence for RADARSAT-1 is much less than that for ERS-1/ERS-2. Over a similar time interval, HH-polarized RADARSAT-1 interferograms have higher coherence than VV-polarized ERS-1/ERS-2 interferograms.

During a very dry season or a period of extremely low water, even swamp forests are potentially exposed to dry ground. Among the interferograms in our study area, patches of swamp forests can lose coherence. This is probably because there was no water beneath the swamp forest. Therefore, the double-bounce backscattering mechanism is diminished, and the dominant backscattering mechanism for "dried" swamp forests become very similar to that for bottomland forests. Alternatively, bottomland forests can be flooded occasionally. The presence of water on bottomland forests produces double-bounce backscattering and, accordingly, makes the radar backscattering return from a bottomland forest similar to that of a swamp forest.

2.6.2 Interferometric Coherence Measurement and Analysis

Only coherent InSAR images enable detection of water-level changes beneath wetlands; hence interferometric coherence variations over the study area are quantitatively assessed. Figure 2.11 shows the InSAR coherence measurements for different land-cover types. Thresholds of complete decorrelation for ERS-1/ERS-2 and RADARSAT-1 interferograms are determined by calculating interferometric coherence values over open water. In Figure 2.11, the coherence measurements from both leaf-on and leaf-off seasons are combined for all classes except for swamp and bottomland forests because seasonality is a critical factor that controls the interferometric coherence of forests. The dependence of the interferometric coherence on a spatial baseline was also explored. For the interferograms used in this study, no dependence between the interferometric coherence and the perpendicular baseline is observed. This is because more than 70% of the interferograms have perpendicular baselines of less than 200 m, and the common spectral band filtering [43] was applied during the interferogram generation.

The coherence over open water is shown in Figure 2.11a. Because open water completely loses coherence for repeat-pass interferometric observations, its coherence value can be regarded as the threshold of complete decorrelation (loss of coherence). The coherence values for both ERS-1/ERS-2 and RADARSAT-1 InSAR images are about 0.06 ± 0013. Therefore, coherence values smaller than 0.1 are deemed as complete decorrelation.

Several sites (Figure 2.3) were chosen to show coherence over urban areas: six of them are located along the Mississippi River, and one is in Morgan City, which is more vegetated than the other urban sites. Figure 2.11b shows interferometric coherence measurements over urban sites from both ERS-1/ERS-2 and RADARSAT-1 interferograms. Overall coherence measurements from both ERS-1/ERS-2 and RADARSAT-1 images are similar, and they are higher than any other land-cover class. However, they vary in the range of about 0.2–0.7. The variations are most likely a result of decorrelation caused by vegetation over the urban areas. Vegetation in urban areas can alter radar backscattering coefficients by more than 8 dB [23]. Urban areas with lower radar backscattering intensities are usually associated with lower interferometric coherence values, suggesting that the vegetation in urban areas causes lower radar backscattering coefficients as well as reduced coherence measurements.

Coherence measurements over agricultural fields are shown in Figure 2.11c. Frequent farming activity with multiple harvests leads to a complete decorrelation in about 100 days. This implies that the vegetation condition of these fields changes completely in about 100 days.

Coherence measurements from swamp forests are shown in Figure 2.11d. The comparison of coherence measurements from ERS-1/ERS-2 and RADARSAT-1 images produces the following inferences:

1. Coherence is higher during leaf-off seasons than during leaf-on seasons for both ERS-1/ERS-2 and RADARSAT-1 images.
2. The coherence from HH-polarization RADARSAT-1 images is generally higher than that from VV-polarization ERS-1/ERS-2 images.

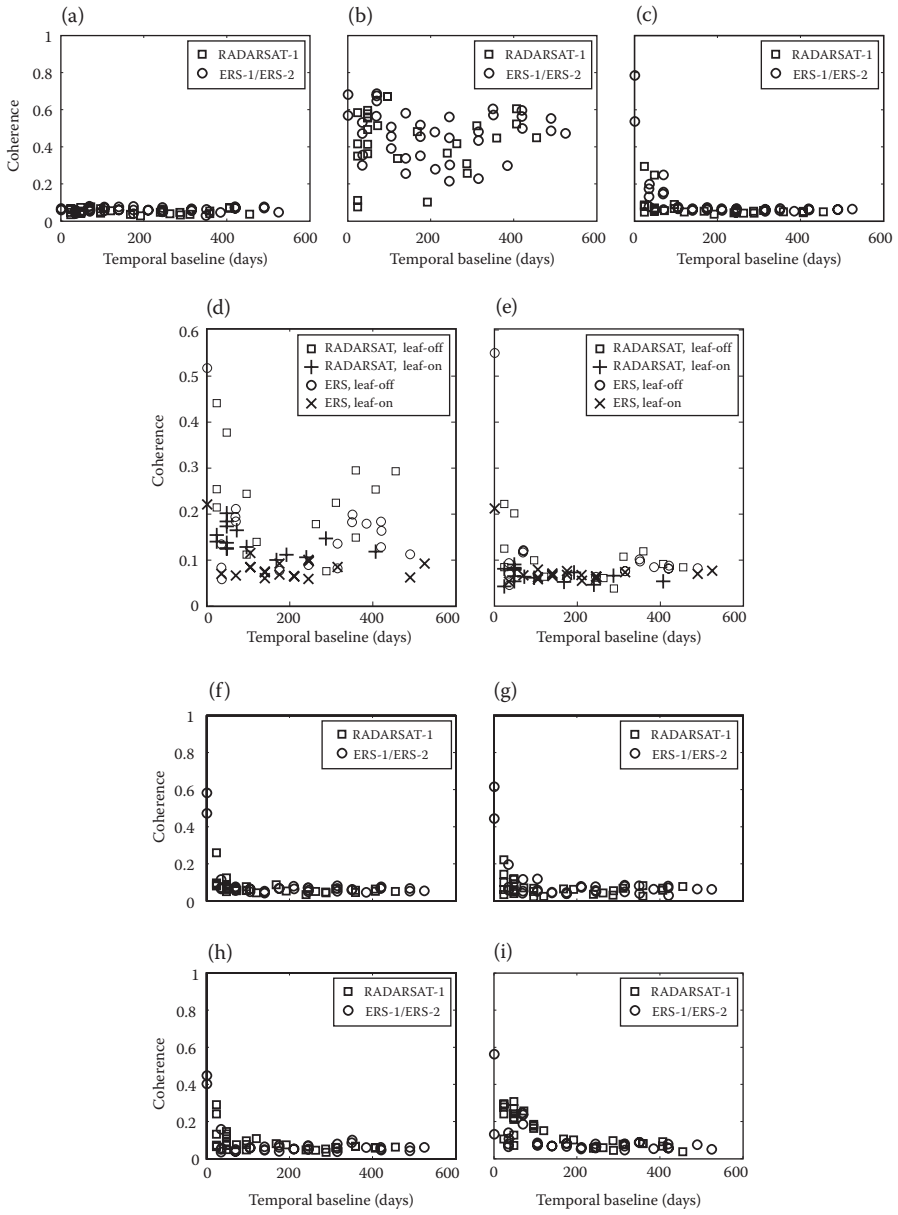

FIGURE 2.11 InSAR coherence as a function of time separation for seven major land-cover classes including (a) open water, (b) urban, (c) agriculture, (d) swamp forest, (e) bottomland forest, (f) freshwater marsh, (g) intermediate marsh, (h) brackish marsh, and (i) saline marsh for both ERS-1/ERS-2 and RADARSAT-1 interferograms acquired during leaf-off and leaf-on seasons. The scale for (d) and (e) is different from others to illustrate that seasonality is one of the factors controlling coherence for forests.

3. The coherence from both RADARSAT-1 images and ERS-1/ERS-2 images during leaf-off season can last over 2 years (Figure 2.11d).

If the scattering elements came primarily from the top of the forest canopy, it is unlikely that the SAR signals are coherent over a period of about 1 month or longer (e.g., [39,40]) because leaves and small branches that make up the forest canopy change due to weather conditions. Based on interferometric coherence (Figure 2.11d) and backscattering coefficient values (Figure 2.11c) during leaf-off and leaf-on seasons, we conclude that the dominant radar backscattering mechanism over swamp forests during the leaf-off seasons is double-bounce backscattering. As a result, RADARSAT-1 and ERS-1/ERS-2 images during leaf-off seasons are capable of imaging water-level changes over swamp forests. During leaf-on seasons, HH-polarization RADARSAT-1 images can maintain coherence for a few months, reaching up to about 0.2. If HH-polarized C-band radar images were acquired for shorter time intervals during leaf-on seasons, they could also be used for measuring water-level changes.

Coherence measurements for bottomland forests are shown in Figure 2.11e. The coherence is higher during leaf-off than leaf-on seasons. The HH-polarization RADARSAT-1 images tend to have higher coherence than the VV-polarized ERS-1/ERS-2 images for short temporal separations (less than about 2 months). The coherence from both ERS-1/ERS-2 and RADARSAT-1 images decreases exponentially with time. ERS-1/ERS-2 images become decorrelated in about 1 month, but RADARSAT-1 can maintain coherence for up to about 2 months (Figure 2.11e). Two major factors affect the difference in radar backscattering and coherence between swamp and bottomland forests. First, the double-bounce backscattering is enhanced over swamp forests. The water beneath trees enhances the double-bounce backscattering for swamp forests, producing high InSAR coherence as well as a high backscattering coefficient. For bottomland forests, forest understory attenuates radar signal returns and the double-bounce backscattering is retarded, resulting in relatively lower coherence as well as smaller backscattering values than swamp forests. Second, there are structural differences between the two forest types. The bottomland forests have broad leaves and deterrent structures where the lateral branches form a wide and bell-shaped crown, which enhances surface and volume backscattering. The above coherence analysis suggests that SAR images, preferably HH-polarized, can maintain good coherence over both swamp and bottomland forests for about 1 month. Accordingly, shorter temporal separations (a few days) will significantly improve the utility of InSAR coherence for the detection of water-level changes.

Coherence measurements over marshes are shown in Figure 2.11f–i. Coherence measurements are generally higher from HH-polarized RADARSAT-1 images than from VV-polarized ERS-1/ERS-2 images; ERS-1/ERS-2 can barely maintain coherence for about 1 month, whereas RADARSAT-1 maintains coherence up to about 3 months. The coherence values for intermediate, freshwater, and brackish marshes are similar, and they are lower than those for saline marshes. Saline marshes have nearly vertical stalks. Freshwater marshes have broadleaf plants that form a mostly vertical canopy and the plants die in the winter but retain the canopy structure until spring turnover and green-up [9]. Overall, saline marshes have the highest coherence

(Figure 2.11i) as well as the highest backscattering value (Figure 2.6) among marsh classes, suggesting that the saline marshes tend to develop more dominant vertical structure than other marshes to allow double-bounce backscattering of C-band radar waves. As marshes can only maintain coherence in less than 24 days, acquiring repeat-pass SAR images over short time intervals (a few days) would help robustly detect water-level changes.

Based on the findings in Sections 2.5 and 2.6, a decision-tree vegetation classification approach is proposed as shown in Figure 2.12. In the classifier, $\langle\rho\rangle$ is the **Q3**

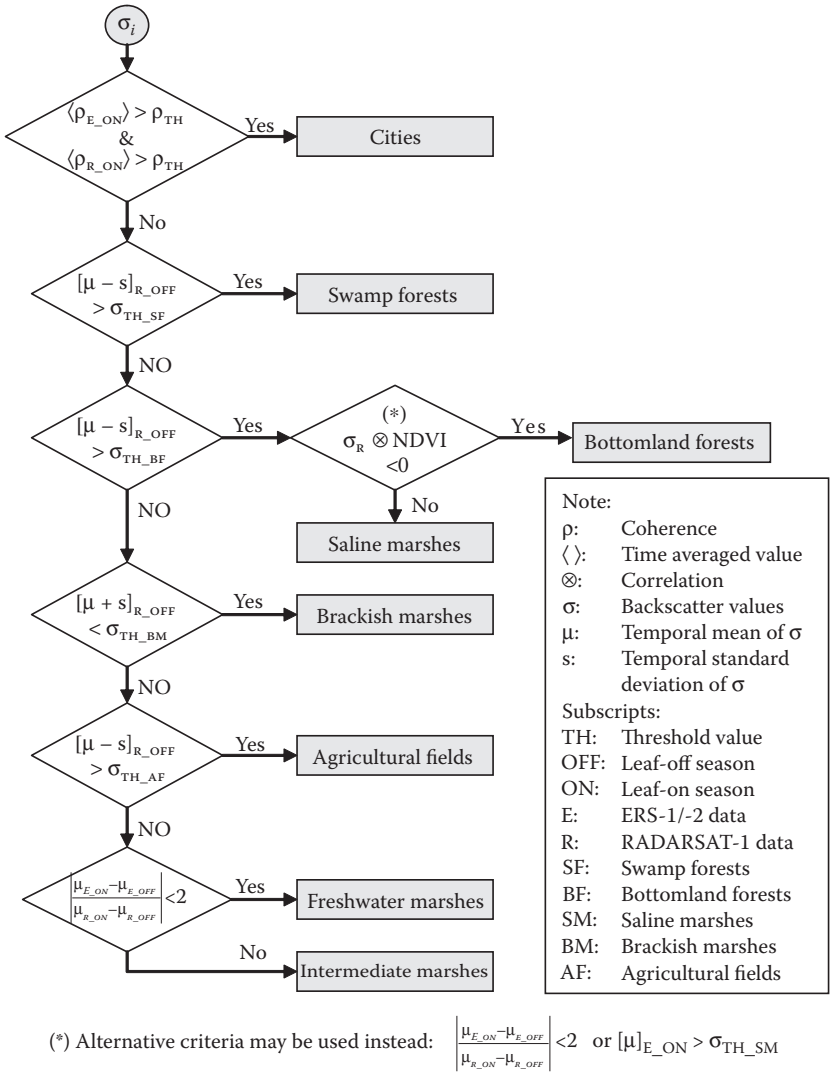

FIGURE 2.12 A decision-tree vegetation classifier based on the findings in Sections 2.5 and 2.6.

TABLE 2.2
Threshold Values for the Decision-Tree Classifier Based on the Data Used in this Study

Parameters	Threshold Values
ρ_{TH}	0.4
σ_{TH_SF}	−6.8 dB
σ_{TH_BF}	−9.5 dB
σ_{TH_SM}	−11.0 dB
σ_{TH_BM}	−12.5 dB
σ_{TH_AF}	−10.5 dB

average coherence value from image pairs with temporal baselines ranging from 1 day through over a year. "$\sigma\otimes$ NDVI" means the computation of correlation coefficient between temporal radar backscatter data and the NDVI data of woody wetlands or deciduous forests. "μ" represents the temporal mean value of "σ," and "s" is the standard deviation of "σ" of the sample under consideration for classification.

The assumptions for this classifier are as follows: (1) multiyear time series ERS-1/ERS-2 and RADARSAT-1 data are available, and the backscatter values are calibrated, (2) season-averaged NDVI values are at least available for woody wetlands and deciduous forests. Given a sample location to classify, the time series of backscatter data should be extracted for both ERS and RADARSAT-1 data. The threshold values noted by the subscript "TH" in Figure 2.12 can be derived based on the discussion in Sections 2.5 and 2.6. For the dataset used in this study, those threshold values are suggested in Table 2.2. **Q4**

2.7 InSAR-DERIVED WATER-LEVEL CHANGES

Examples of coherent RADARSAT-1 interferograms with short temporal separations are shown in Figure 2.13. These interferograms are unwrapped to remove the intrinsic ambiguity of 2π in phase measurements (e.g., [25]), and interferometric phase values are used to study changes in the water level of swamp forests. Each interferogram shows the relative changes in water level between dates when the two images were acquired. Each fringe represents a range (distance from the satellite to ground) change of about 3.20 cm water-level change for RADARSAT-1 images. From the interferograms in Figure 2.13, the following inferences are made:

2.7.1 Water-Level Changes are Dynamic

Water-level changes reach as much as 50 cm over a distance of about 40 km (Figure 2.13b). The direction and the density of fringes within the Atchafalaya Basin vary spatially. Such changes in water level reflect local differences in topographic

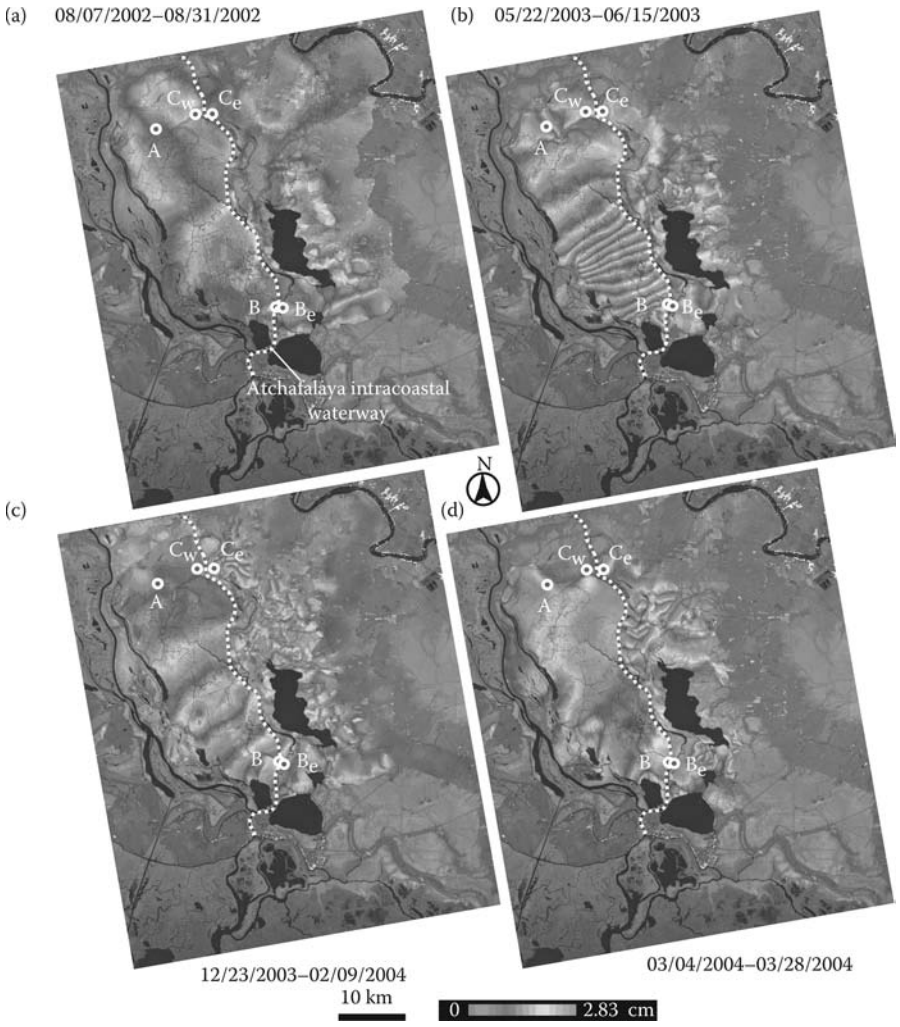

FIGURE 2.13 **(See color insert following page xxx.)** Unwrapped RADARSAT-1 images of the Atchatalaya Basin are used to quantify water-level changes over Atchafalaya Basin Floodway. InSAR-derived water-level changes at the selected locations are compared with gage readings (see Table 2.3 for details).

constrictions and vegetation resistance to the surface flow. Flooding throughout this area is primarily by sheet flow after the rivers and bayous leave their banks. Under ideal circumstances, water should flow placidly and smoothly over a symmetrically smooth surface devoid of obstructions. Thus, the sheet flow should not be symmetric throughout the study area, that is, it should not be a smooth, even surface of constant elevation from one edge of the swamp to the other. Instead, a water surface with bulges and depressions reflecting the topographic constrictions and vegetation resistance in sheet flow is ideal.

2.7.2 Water-Level Changes are Heterogeneous

First, the observed fringes exhibit evidence of control by structures such as levees, canals, bayous, and roads, resulting in abrupt changes in interferometric phase value. The heterogeneity in water-level change is due primarily to these man-made structures and artificial boundaries. Second, within the ABF, the observed interferometric fringes are bent. This suggests that local variations in vegetation cover resist water flow variably. Heterogeneous water-level changes such as these make it impossible to accurately characterize water storage based on measurements from a few sparsely distributed gauge measurements. This demonstrates the unique capability of InSAR to map water-level changes in unprecedented spatial detail. This is the most promising aspect of mapping water-level changes with InSAR. Q5

2.7.3 Interferograms Reveal Both Localized and Relatively Large-Scale Water-Level Changes

On one hand, for example, localized changes in water flow are evident in the 24-h interferogram (outlined in white in Figure 2.10a) and the 35-day interferogram during March–April 1998 (outlined in white in Figure 2.10b). On the other, relatively large-scale changes in water level are observed across much of the water basin (e.g., Figure 2.13b and c).

The interferometric fringes are dissected by rivers, canals, levees, roads, and other structures; therefore, the interferometric phase measurements are perhaps disconnected at these boundaries. In other words, interferometric phase measurements at two nearby pixels separated by these boundaries are discontinuous. This adds enormous complexity to understanding water-level changes inferred from InSAR measurements. Furthermore, calculating water-level changes along two different paths that are separated by these boundaries may lead to different estimates.

The RADARSAT-1 interferograms (Figure 2.13) are used to illustrate this. The interferograms are first unwrapped piecewise. In particular, the regions to the west and east of the Atchafalaya Intracoastal Waterway (AICWW) were unwrapped separately. The interferometric coherence along the AICWW is often lost. To investigate water-level changes quantitatively, several locations including two gauge locations (Cross Bayou station at A and Sorrel station at B) were selected. Both A and B lie within the swamp forests west of the AICWW, and the phase measurements at the exact locations of A and B can be extracted. To the east of B and across the AICWW, a location B_e (Figure 2.13) over the swamp forest east of the AICWW, where InSAR coherence is maintained, is chosen. Finally, a location C in the upper portion of the AICWW (Figure 2.13) is selected. The interferometric coherence is not maintained at C; therefore, two locations immediately adjacent to C are chosen: one is over the swamp forest to the west of the AICWW (C_w in Figure 2.13) and the other, over the swamp forest to the east of AICWW (C_e in Figure 2.13). Interferometric coherence is maintained at C_w and C_e, and consequently InSAR phase values at these two points are extractable.

First, the water-level changes measured by InSAR are compared with those recorded at gages at A and B to validate the reliability of the InSAR-based measurements of water-level changes. Table 2.3 summarizes the results of water-level changes

TABLE 2.3
Comparison of Water-Level Change Measurements between InSAR and Gage Stations

Date	InSAR Measurements A–B (cm)	Gage Readings A–B (cm)	InSAR Measurements C_w–B (cm)	InSAR Measurements C_e–B_e (cm)
08/07/2002–08/31/2002	–0.01	–0.60	–1.38	–2.01
05/22/2003–06/15/2003	36.10	N/A	31.34	6.61
12/23/2003–02/09/2004	13.63	11.44	13.99	1.34
03/04/2004–03/28/2004	3.99	5.19	5.68	–0.96

Notes: A and B are two gage stations within the swamp forest west of the AICWW (Figure 2.13). C is a point over the AICWW, and InSAR images are not coherent at this location. C_w and C_e, two coherent points near C, are located over the swamp forests west and east of the AICWW, respectively. B_e is a point adjacent to B. Both C_w and B are within the swamp forest west of the AICWW, and C_e and B_e are over the swamp forest east of the AICWW (Figure 2.13).

from gages and from the interferograms in Figure 2.13. The InSAR-derived water-level changes at A and B are in good agreement with gage readings and within about 2 cm overall discrepancy. This indicates that water-level change measurements by InSAR are probably as good as those of the gages. We can infer that the InSAR-detected water-level changes in non-gage areas are trustworthy. If this is the case, then the InSAR technique provides a unique way to map dynamic and heterogeneous water-level changes at accuracies comparable to gages and at a spatial resolution unattainable by gages. The gage data at Cross Bayou (A in Figure 2.13) on May 22, 2003, do not exist, so one could not confirm water-level changes of about 36 cm detected by InSAR (Figure 2.13b). If the perceived correspondence of about 2 cm between InSAR and gage measurements is extended, the gage reading at A can be estimated to be about 437 cm on May 22, 2003. This demonstrates the utility of InSAR-based water-level change measurement to augment the missing gage data. InSAR measures relative elevation changes between image acquisition dates; hence, it requires calibration with respect to absolute water-level measurements. For the Achafalaya Basin, the gage station over the swamp forest is used for the absolute water-level change calibration. Combining the InSAR image (Figure 2.13c) and the gage station reading, one can, therefore, derive volumetric water storage change during 12/23/2003 and 2/9/2004 (Figure 2.14).

Next, the water-level changes measured along two different paths (C_w–B and C_e–B_e) within two swamp forest bodies separated by the AICWW are compared. Please note that locations C_w and B are within the swamp forest west of the AICWW and locations C_e and B_e are within the swamp forest east of the AICWW. Integrating interferometric phase measurements along the western path (C_w–B) and the eastern path (C_e–B_e) gives different water-level changes that depend on the path (Table 2.3). This is interpreted as the result of structures that obstruct smooth and rapid water flow, primarily within the swamp forests west of the AICWW. The change in fringe

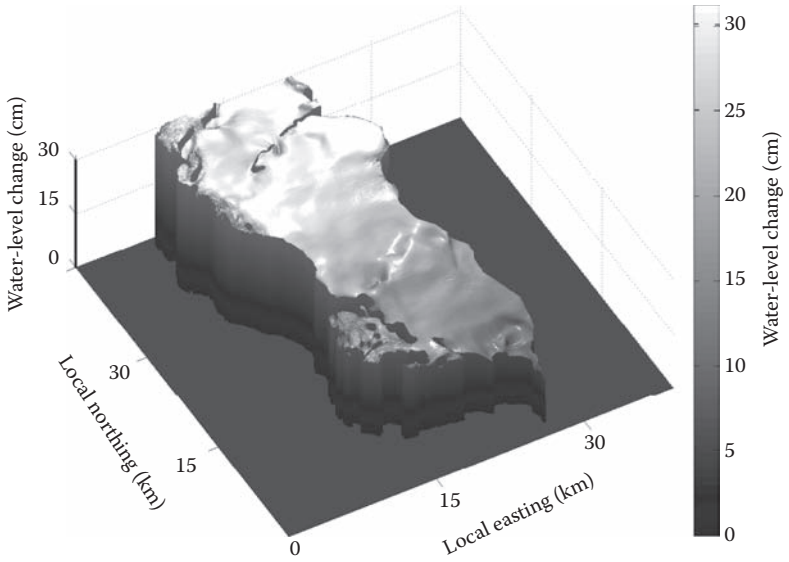

FIGURE 2.14 Volumetric rendering of absolute water-level changes over the portion of swamp forests west of the AICWW during December 23, 2003 and February 9, 2004, derived from the InSAR image in Figure 2.13c.

pattern across the AICWW suggests that parts of the AICWW also act as barriers to continuous water flow in this area. Water-level changes in swamp forests over the study area are heterogeneous and disconnected by structures and other barriers and therefore not represented adequately by sparsely distributed gage stations. This finding is useful for hydrologists to enhance surface water flow models by correctly defining the spatial extent of homogeneous continuum and for emergency planners to simulate the dynamics of flood waters in the region with enhanced accuracy.

2.8 DISCUSSIONS AND CONCLUSION

Multitemporal RADARSAT-1 and ERS SAR images over southern Louisiana are used to study characteristics of the radar backscattering coefficient over vegetation classes. Calibrated radar backscattering coefficients over six land-cover classes—bottomland forest, swamp forest, freshwater marsh, intermediate marsh, brackish marsh, and saline marsh—provide insights about the relationship between seasonal variation of σ° and vegetation canopy structure. Double-bounced backscattering is the dominant scattering mechanism for swamp forests and saline marshes. Volume backscattering dominates freshwater and intermediate marshes and bottomland forests. Brackish marshes are likely dominated by volume backscattering and specular scattering. RADARSAT-1 backscattering coefficients offer better separability among different wetland land-cover types than ERS data, suggesting that C-band HH polarization is more sensitive to structural differences than C-band VV polarization.

Radar backscattering coefficients during leaf-off seasons have strong correlations with NDVI. Swamp and bottomland forests show negative correlations between NDVI and SAR data, while marshes exhibit positive correlations with RADARSAT data only. The correlation between σ° and NDVI is useful in differentiating between forests and coastal marshes and in refining our understanding of vegetation structure.

Wherever InSAR coherence is maintained, InSAR's utility to map water-level changes at high spatial resolution makes it an attractive tool for studying many hydrological processes. Adequately characterizing the heterogeneous water-level changes over a complex wetland system requires many ground-based measurements, which are cost-prohibitive. In this chapter, C-band InSAR images have proved useful for mapping water-level changes of coastal wetlands in Louisiana. Particularly, HH-polarized C-band InSAR can maintain good coherence for mapping water-level changes over coastal wetlands if the SAR images are acquired in a few days. The L-band InSAR images generally maintain much higher coherence than C-band InSAR; therefore, it is expected that L-band InSAR can be used to map water-level changes over denser forests.

Figure 2.15a and b shows two interferograms over the study area. Figure 2.15a is a 46-day L-band ALOS PALSAR interferogram acquired from HH-polarized images acquired on February 27 and April 14, 2007, and Figure 2.15b is a 24-day C-band RADARSAT-1 interferogram acquired from HH-polarized SAR images acquired on March 4 and 28, 2004. This study shows that the 46-day L-band interferogram is generally more coherent than the 24-day C-band interferogram, which can maintain relatively higher coherence than VV-polarized C-band ERS/ENVISAT images as demonstrated in the previous sections. Particularly, the L-band PALSAR interferogram can maintain coherence over bottomland forests and marshes where C-band coherence is often lost (Figure 2.15b). Therefore, L-band interferograms allow robust monitoring of water-level changes over coastal wetlands due to the higher coherence. Ultimately, combining C-band and L-band InSAR images can significantly improve temporal sampling of water-level measurements.

However, there are at least two shortfalls regarding water-level measurements from InSAR images. First, InSAR requires the presence of emergent vegetation [27–29,33,44] or structures in water [51] to allow radar signals to be scattered back to the antenna to measure water-level change. Over open-water bodies, InSAR is useless for detecting water-level change. Second, a repeat-pass InSAR image measures the relative spatial gradient of water-level change between two time periods. In other words, from interferometric phase measurements alone, the absolute volumetric change of water storage within a wetland is not derivable without additional constraints. In a simple case, for example, let us assume the water level over a wetland moves up or down by a constant height. The volumetric change of the wetland can be calculated by the area of the wetland and the constant water-level change. However, an InSAR image can only exhibit a constant phase shift with an ambiguity of multiples of 2π. This can be mistakenly interpreted as being no water-level changes. To estimate the volumetric change of water storage, the absolute water-level change at a single location with a wetland body is required. The situation can become even more complicated if the wetland system consists of many wetland bodies, which are

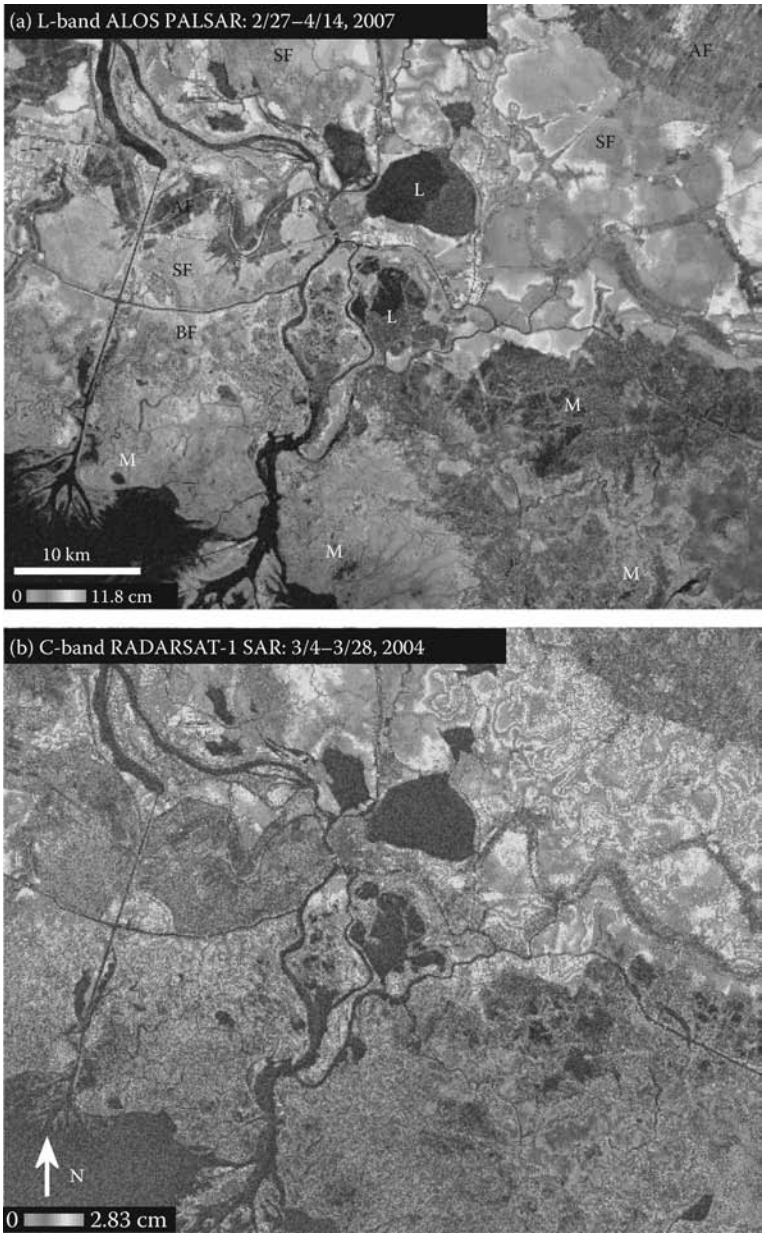

FIGURE 2.15 **(See color insert following page xxx.)** (a) L-band ALOS and (b) C-band RADARSAT-1 InSAR images showing water-level changes in coastal wetlands over southeastern Louisiana. Each fringe (full color cycle) represents a line-of-sight range change of 11.8 and 2.83 cm for ALOS and RADARSAT-1 interferograms, respectively. Interferogram phase values are unfiltered for coherence comparison and are draped over the SAR intensity image of the early date. Areas of loss of coherence are indicated by random colors. M: marshes (freshwater, intermediate, brackish, and saline marshes); L: lake, SF: swamp forest; BF: bottomland forest; AF: agricultural field.

bounded by anthropogenic structures such as levees and canals, which can disconnect the InSAR phase changes. In this case, it may be impossible to estimate volumetric storage change of the whole wetland system without knowing the absolute water-level change in each wetland body.

A more feasible solution is to include water-level measurements from a radar altimeter with adequate spatial resolution and vertical accuracy, such as the Water And Terrestrial Elevation Recovery (WATER) satellite mission [52]. Similar to the Shuttle Radar Topography Mission (SRTM), WATER is a dual-antenna radar interferometer that can achieve centimeter-level height accuracy at tens of meters spatial resolution. A similar system will not only provide temporal and spatial variations of water-level height but also provide measurements to facilitate the use of InSAR measurements over wetlands from other satellite radar imagery. Optimized radar images with short repeat-pass acquisitions from multiple satellite sensors, combined with available ground-based gage readings, will improve the characterization of surface water hydraulics, hydrological modeling predictions, and the assessment of future flood events over wetlands.

ACKNOWLEDGMENTS

ERS-1/ERS-2 SAR images are copyright ©1992–1998 European Space Agency (ESA) and were provided by ESA and Eurimage. RADARSAT-1 images are copyright ©2002–2004 Canadian Space Agency and were provided by Alaska Satellite Facility (ASF). PALSAR data are copyright JAXA/METI 2007 and were provided by ASF. This research was supported by funding from the U.S. Geological Survey (USGS) Director Venture Capital Fund, USGS Eastern Region Venture Capital Fund, USGS Land Remote Sensing Program, NASA Solid Earth and Natural Hazards Program. We thank ASF and ESA for their support in programming SAR data acquisitions and delivering data timely. We thank Christopher Swarzenski (USGS) for providing us the water-level readings at gauge stations used in this study, and Kurtis Nelson and Bhaskar Ramachandran for technical reviews and comments.

REFERENCES

1. Karszenbaum, H., et al., ERS-2, RADARSAT SAR backscattering characteristics of the Parana River Delta Wetland, Argentina, Special Publication SP-461, 2000. **Q6**
2. USACE, *Louisiana Ecosystem Restoration Study: Louisiana Coastal Area (LCA)*, http://www.lca.gov/final_report.aspx, 2004.
3. LCWCRTF/WCRA, *Coast 2050: Toward a Sustainable Coastal Louisiana*, Louisiana Department of Natural Resources, Baton Rouge, LA, 1998, p. 161.
4. Barras, J., et al., Historical and projected coastal Louisiana land changes: 1978–2050, USGS Open File Report 03-334, 2003, p. 39.
5. Coe, M., A linked global model of terrestrial hydrologic processes: Simulation of the modern rivers, lakes, and wetlands, *J. Geophys. Res.*, 103, 8885, 1998.
6. Alsdorf, D., Lettenmaier, D., and Vörösmarty, C., The need for global, satellite-based observations of terrestrial surface waters, *EOS Trans.*, 84, 269, 2003.
7. Ramsey, E.W., III, Monitoring flooding in coastal wetlands by using radar imagery and ground-based measurements, *Int. J. Remote Sens.*, 16, 2495, 1995.

8. Ramsey, E.W., III, Radar remote sensing of wetlands, In: R.S. Lunetta and C.D. Elvidge (Eds), *Remote Sensing Change Detection*, Ann Arbor Press, Chelsea, MI, 1999, p. 211.
9. Ramsey, E.W., III, et al., Multiple baseline radar interferometry applied to coastal land cover classification and change analyses, *IEEE Trans. Geosci. Remote Sens.*, 43, 283, 2006. **Q7**
10. Grings, F.M., et al., Monitoring flood condition in marshes using EM models and ENVISAT ASAR observations, *IEEE Trans. Geosci. Remote Sens.*, 44, 936, 2006.
11. Costa, M.P.F., Use of SAR satellites for mapping zonation of vegetation communities in the Amazon floodplain, *Int. J. Remote Sens.*, 25, 1817, 2004.
12. Costa, M.P.F., et al., Biophysical properties and mapping of aquatic vegetation during the hydrological cycle of the Amazon floodplain using JERS-1 and RADARSAT, *Int. J. Remote Sens.*, 23, 1401, 2002.
13. Hess, L.L. and Melack, J.M., Mapping wetland hydrology and vegetation with synthetic aperture radar, *Int. J. Ecol. Environ. Sci.*, 20, 197, 1994.
14. Hess, L.L., et al., Delineation of inundated area and vegetation along the Amazon floodplain with the SIR-C synthetic aperture radar, *IEEE Trans. Geosci. Remote Sens.*, 33, 896, 1995.
15. Kasischke, E.S. and Bourgeau-Chavez, L.L., Monitoring south Florida wetlands using ERS-1 SAR imagery, *Photogrammetric Eng. Remote Sens.*, 63, 281, 1997.
16. Le Toan, T., et al., Rice crop mapping and monitoring using ERS-1 data based on experiment and modeling results, *IEEE Trans. Geosci. Remote Sens.*, 35, 41, 1997.
17. Baghdadi, N., et al., Evaluation of C-band SAR data for wetlands mapping, *Int. J. Remote Sens.*, 22, 71, 2001.
18. Bourgeau-Chavez, L.L., et al., Analysis of space-borne SAR data for wetland mapping in Virginia riparian ecosystems, *Int. J. Remote Sens.*, 22, 3665, 2001.
19. Simard, M., et al., Mapping tropical coastal vegetation using JERS-1 and ERS-1 radar data with a decision tree classifier, *Int. J. Remote Sens.*, 23, 1461, 2002.
20. Townsend, P.A., Estimating forest structure in wetlands using multitemporal SAR, *Remote Sens. Environ.*, 79, 288, 2002.
21. Bourgeau-Chavez, L.L., et al., Remote monitoring of regional inundation patterns and hydroperiod in the greater Everglades using synthetic aperture radar, *Wetlands*, 25, 176, 2005.
22. Kiage, L.M., et al., Applications of RADARSAT-1 synthetic aperture radar imagery to assess hurricane-related flooding of coastal Louisiana, *Int. J. Remote Sens.*, 26, 5359, 2005.
23. Kwoun, O. and Lu, Z., Multi-temporal RADARSAT-1 and ERS Backscattering Signatures of Coastal Wetlands at Southeastern Louisiana, *Photogrammetric Eng. Remote Sens.*, 75, in press. **Q8**
24. Massonnet, D. and Feigl, K., Radar interferometry and its application to changes in the Earth's surface, *Rev. Geophys.*, 36, 441, 1998.
25. Rosen, P., et al., Synthetic aperture radar interferometry, *Proc. IEEE*, 88, 333, 2000.
26. Lu, Z., Kwoun, O., and Rykhus, R., Interferometric synthetic aperture radar (InSAR): Its past, present and future, *Photogrammetric Eng. Remote Sens.*, 73, 217, 2007.
27. Alsdorf, D., et al., Interferometric radar measurements of water level changes on the Amazon floodplain, *Nature*, 404, 174, 2000.
28. Alsdorf, D., et al., Water level changes in a large Amazon lake measured with space-borne radar interferometry and altimetry, *Geophys. Res. Lett.*, 28, 2671, 2001.
29. Wdowinski, S., et al., Space-based measurements of sheet-flow characteristics in the Everglades wetland, Florida, *Geophys. Res. Lett.*, 31, L15503, doi: 10.1029/2004GL020383, 2004.
30. Richards, J., Woodgate, P., and Skidmore, A., An explanation of enhanced radar backscattering from flooded forests, *Int. J. Remote Sens.*, 8, 1093–1100, 1987.

31. Beaudoin, A., et al., Retrieval of forest biomass from SAR data, *Int. J. Remote Sens.*, 15, 2777, 1994.
32. Wang, Y., et al., Understanding the radar backscattering from flooded and nonflooded Amazonian forests: Results from canopy backscatter modeling, *Remote Sens. Environ.*, 54, 324, 1995.
33. Lu, Z., et al., C-band radar observes water-level change in swamp forests, *EOS Trans. AGU*, 86, 141, 2005.
34. Nelson, S.A.C., Soranno, P.A., and Qi, J., Land-cover change in upper Barataria Basin Estuary, Louisiana, 1972–1992: Increase in wetland area, *Environ. Manag.*, 29, 716, 2002.
35. Chabreck, R.H., Vegetation, water, and soil characteristics of the Louisiana coastal region, *LSU Agric. Exp. Stn. Bull.*, 664, 1, 1972.
36. Barras, J., et al., *Types of Wetlands*, http://www.americaswetlandresources.com/wildlife_ecology/plants_animals_ecology/wetlands/TypesofWetlands.html, 2006.
37. IFAS, *Forest Ecosystems*, http://www.sfrc.ufl.edu/4h/Ecosystems/ecosystems.html, 2006.
38. Ulaby, F.T. and Dobson, C.M., *Handbook of Radar Scattering Statistics for Terrain*, Artech House, Inc., Norwood, MA, 1989, p. 357.
39. Hagberg, J., Ulander, L., and Askne, J., Repeat-pass SAR interferometry over forested terrain, *IEEE Trans. Geosci. Remote Sens.*, 33, 331, 1995.
40. Wegmüller, U. and Werner, C., Retrieval of vegetation parameters with SAR interferometry, *IEEE Trans. Geosci. Remote Sens.*, 35, 18, 1997.
41. Zebker, H.A. and Villasenor, J., Decorrelation in interferometric radar echoes, *IEEE Trans. Geosci. Remote Sens.*, 30, 950, 1992.
42. Lu, Z. and Freymueller, J., Synthetic aperture radar interferometry coherence analysis over Katmai volcano group, Alaska, *J. Geophys. Res.*, 103, 29887, 1998.
43. Gatelli, F., et al., The wavenumber shift in SAR interferometry, *IEEE Trans. Geosci. Remote Sens.*, 32, 855, 1994.
44. Lu, Z. and Kwoun, O., RADARSAT-1 and ERS interferometric coherence analysis over southeastern coastal Louisiana: Implication for mapping water-level changes beneath swamp forests, *IEEE Trans. Geosci. Remote Sens.*, 46, 2167, 2008.
45. Wegmüller, U. and Werner, C., GAMMA MSP reference manual, *Gamma Remote Sensing*, 2003. **Q9**
46. Frost, V.S., et al., A model for radar images and its application to adaptive digital filtering of multiplicative noise, *IEEE Trans. Pattern Anal. Machine Intell.*, PAMI-4, 157, 1982.
47. USGS-NWRC, *2004 Digital Orthophoto Quarter Quadrangles for Louisiana*, http://www.lacoast.gov/maps/2004doqq/index.htm, 2005.
48. Meadows, P.J., Rosich, B., and Santella, C., The ERS-2 SAR performance: The first 9 years, in *Proceedings of the ENVISAT and ERS Symposium*, Salzburg, Austria, September 6–10, 2004.
49. Ferretti, A., Prati, C., and Rocca, F., Permanent scatterers in SAR interferometry, *IEEE Trans. Geosci. Remote Sens.*, 39, 8, 2001.
50. Sellers, P.J., Canopy reflectance, photosynthesis, and transpiration, *Int. J. Remote Sens.*, 6, 1335, 1985. **Q10**
51. Kim, S.-W., Hong, S.-H., and Won, J.-S., An application of L-band synthetic aperture radar to tide height measurement, *IEEE Trans. Geosci. Remote Sens.*, 43, 1472, 2005.
52. Alsdorf, D., Rodríguez, E., and Lettenmaier, D., Measuring surface water from space, *Rev. Geophys.*, 45, RG2002, doi: 10.1029/2006RG000197, 2007.